Topology and Sizes of HII Regions during Cosmic Reionization

Article (Published Version)

Monthly Notices
of the
ROYAL ASTRONOMICAL SOCIETY

Mon. Not. R. Astron. Soc. **413,** 1353–1372 (2011) doi:10.1111/j.1365-2966.2011.18219.x

Topology and sizes of H II regions during cosmic reionization

Martina M. Friedrich,[1⋆] Garrelt Mellema,[1] Marcelo A. Alvarez,[2] Paul R. Shapiro[3] and Ilian T. Iliev[4]

[1]*Department of Astronomy & Oskar Klein Centre, AlbaNova, Stockholm University, SE-106 91 Stockholm, Sweden*
[2]*Canadian Institute for Theoretical Astrophysics, University of Toronto, 60 St George Street, Toronto, ON M5S 3H8, Canada*
[3]*Department of Astronomy and the Texas Cosmology Center, The University of Texas at Austin, TX 78712, USA*
[4]*Astronomy Centre, Department of Physics & Astronomy, Pevensey II Building, University of Sussex, Falmer, Brighton BN1 9QH*

Accepted 2010 December 16. Received 2010 December 13; in original form 2010 June 9

ABSTRACT

We use the results of large-scale simulations of reionization to explore methods for characterizing the topology and sizes of H II regions during reionization. We use four independent methods for characterizing the sizes of ionized regions. Three of them give us a full size distribution: the friends-of-friends (FoF) method, the spherical average (SPA) method and the power spectrum (PS) of the ionized fraction. The latter three methods are complementary: while the FoF method captures the size distribution of the small-scale H II regions, which contribute only a small amount to the total ionization fraction, the SPA method provides a smoothed measure for the average size of the H II regions constituting the main contribution to the ionized fraction, and the PS does the same while retaining more details on the size distribution. Our fourth method for characterizing the sizes of the H II regions is the average size which results if we divide the total volume of the H II regions by their total surface area (i.e. $3V/A$), computed in terms of the ratio of the corresponding Minkowski functionals of the ionized fraction field. To characterize the topology of the ionized regions, we calculate the evolution of the Euler characteristic. We find that the evolution of the topology during the first half of reionization is consistent with inside-out reionization of a Gaussian density field. We use these techniques to investigate the dependence of the size and topology on some basic source properties, such as the halo mass-to-light ratio, susceptibility of haloes to negative feedback from reionization and the minimum halo mass for sources to form. We find that the suppression of ionizing sources within ionized regions slows the growth of H II regions and also changes their size distribution. Additionally, the topology of simulations including suppression is more complex, as indicated by the evolution of the Euler characteristic of the ionized regions. We find the density and ionized fraction to be correlated on large scales, in agreement with the inside-out picture of reionization.

Key words: ISM: bubbles – H II regions – galaxies: formation – galaxies: high-redshift – intergalactic medium – cosmology: theory.

1 INTRODUCTION

The cosmic microwave background (CMB) discovered in 1965 was evidence that the hot big bang Universe cooled and recombined (Penzias & Wilson 1965). That same year, however, the intergalactic medium (IGM) at $z = 2$ was found to be largely devoid of neutral hydrogen atoms, when astronomers failed to detect their Lyman α resonant scattering in the spectra of the first quasars discovered with high enough redshift to make the transition visible from the ground (Gunn & Peterson 1965; Oke 1966). This was soon interpreted to mean that, unless the IGM were many orders of magnitude less dense than the average density of a critical universe, most of the hydrogen atoms there must have been reionized sometime between $z = 1000$ and 2.

Although we have since then learned much more about both the CMB and the H I absorption towards high-redshift quasi-stellar objects (QSOs), currently, it is still those two observables which constrain the epoch of reionization (EoR). The results from the *WMAP* measurements of the CMB have constrained the optical depth due to electron scattering, $\tau_{\rm es}$, to 0.088 ± 0.015, implying that an instantaneous reionization would have happened at $z = 10.4 \pm 1.2$

⋆E-mail: martina@astro.su.se

(Komatsu et al. 2011). The QSO spectra obtained within the Sloan Digital Sky Survey indicate a low, but rapidly rising neutral fraction around redshift 6 (Fan et al. 2006; Willott et al. 2007). The combination of these two measurements suggests that the EoR extended over several redshift units.

However, a series of measurements are being performed or prepared that are expected to give completely new constraints on this early epoch of galaxy formation. Radio telescopes capable of measuring at low frequencies (GMRT[1], 21CMA,[2] LOFAR,[3] MWA,[4] PAPER[5]) should be able to detect the signature of redshifted 21-cm radiation from neutral hydrogen during the EoR. These measurements are challenging due to the presence of the strong foreground emission of, mostly, our own Milky Way as well as ionospheric distortions. If successful, these experiments should produce a detection before the 50th anniversary of the discovery of the CMB and the Gunn–Peterson effect.

In preparation for these 21-cm observations, many groups have been numerically simulating the reionization process on large scales (Iliev et al. 2006a; McQuinn et al. 2007; Shin et al. 2008, to name a small selection; also see Trac & Gnedin 2009 for a review on simulations of reionization). Seminumerical models have also been developed, first by Zahn et al. (2007), later improved by others (Mesinger & Furlanetto 2007; Santos et al. 2008; Alvarez et al. 2009; Choudhury, Haehnelt & Regan 2009; Alvarez & Abel 2010; Mesinger, Furlanetto & Cen 2011). What both these types of calculations give us is the evolution of the ionized fraction of intergalactic hydrogen in the universe, $x(\boldsymbol{r}, t)$.

The simulation results show a great amount of complexity in $x(\boldsymbol{r}, t)$. As the sources of reionization are likely to be clustered in space, individual H II regions typically contain many sources (e.g. Furlanetto, Zaldarriaga & Hernquist 2004; Iliev, Scannapieco & Shapiro 2005; Iliev et al. 2006b) and obtain complex shapes in three-dimensional space. Rare sources are more biased than more abundant ones, and it is expected that the level of bias will largely determine the characteristic scale of the reionization process (Furlanetto, McQuinn & Hernquist 2006; Iliev et al. 2006b). Accurate theoretical predictions for the morphology and size of H II regions depend upon an understanding of the abundance and clustering of the ionizing sources themselves, in addition to the underlying inhomogeneous density field. A quantitative analysis of the distribution of ionized material during the EoR is thus not a trivial matter and likely several different approaches have to be combined. The main aim of this paper is to describe and evaluate different methods for analysing the properties of the ionization fraction field $x(\boldsymbol{r}, t)$ and its evolution.

The planned observations of the 21-cm line of neutral hydrogen are expected to constrain the ionization fraction field $x(\boldsymbol{r}, t)$ statistically as the power spectrum (PS) of neutral hydrogen fluctuations is the most directly observed quantity via 21-cm radio observations (e.g. Zaldarriaga, Furlanetto & Hernquist 2004; Mellema et al. 2006a; Harker et al. 2010). Future observations, for example, with the SKA may have enough sensitivity to actually image the redshifted 21-cm signal as a function of frequency and thus reveal the spatial structure of the ionization fraction field $x(\boldsymbol{r}, t)$.

[1] Giant Metrewave Telescope, http://gmrt.ncra.tifr.res.in
[2] 21 Centimeter Array, http://21cma.bao.ac.cn
[3] Low Frequency Array, http://www.lofar.org
[4] Murchison Widefield Array, http://www.mwatelescope.org
[5] Precision Array to Probe the Epoch of Reionization, http://astro.berkeley.edu/∼dbacker/eor

Ultimately, we are less interested in the function $x(\boldsymbol{r}, t)$ itself but more in 'why it is like it is', that is, in the properties of the sources and sinks of reionization. For this, one has to find out how the statistical properties of ionization fraction field depend on different source and sink properties. Simulations of reionization can thus be said not to aim at reproducing the actual $x(\boldsymbol{r}, t)$, but rather at showing the same statistical behaviour as the real EoR because, on the one hand, only statistical quantities can be measured (as mentioned above), while, on the other hand, the input of simulations is only statistically comparable to the real conditions.

This paper has two parts. In the first part, we investigate the usefulness, in terms of characterizing size distributions of ionized regions, of different kinds of statistics [e.g. the PS of $x(\boldsymbol{r}, t)$] of a simulated ionization fraction field. In the second part, we employ these statistics to investigate the effect of different source properties. This is useful to draw conclusions on the sources, once statistical properties of the real $x(\boldsymbol{r}, t)$ of reionization can be measured.

We focus on the early and intermediate stages of reionization, when the morphology of H II regions is most well defined and the photon mean-free-path is determined by the patchiness of the reionization process itself. At the latest stages of the reionization process, after overlap, fluctuations in the ultraviolet background are expected to be sensitive to the small fraction of gas which is left neutral in the form, for example, of Lyman-limit systems (Miralda-Escudé, Haehnelt & Rees 2000; Gnedin & Fan 2006; Alvarez & Abel 2010; Prochaska, O'Meara & Worseck 2010). We limit ourselves to analysing the ionization fraction fields $x(\boldsymbol{r}, t)$ from the simulations, not on producing the observable quantities. This is the necessary first step before proceeding to evaluate whether different scenarios can be observationally distinguished. The observables will be discussed in a follow-up paper (Iliev et al., in preparation).

In terms of sections, this paper is organized as follows. Section 2 introduces the simulations included in this study. Section 3 introduces the analysis methods used to investigate these simulations. In Section 4, we test the effect of numerical parameters on the statistics of $x(\boldsymbol{r}, t)$. In Section 5, we test the effect of source properties on the statistics of $x(\boldsymbol{r}, t)$. We end with our conclusions in Section 6.

2 SIMULATIONS

Our simulation methodology has been previously described in detail (Iliev et al. 2006b; Mellema et al. 2006b; Iliev et al. 2007). Here, we will briefly summarize the underlying N-body simulations that were performed and the set of radiative transfer simulations that we analyse. On the scales of interest to us here, the IGM and dark matter followed each other as the cosmic structure arose in the Λ cold dark matter (ΛCDM) universe during this epoch. Even during reionization, since ionization fronts which reionized the IGM moved supersonically, the back reaction of the gas due to mass motions related to pressure forces can be neglected to first approximation (Shapiro & Giroux 1987) and hence the radiative transfer can be done as a post-processing of the N-body density field.

2.1 *N*-body simulations

As a basis for our radiative transfer calculations, we begin with the time-dependent density field extracted from N-body simulations of structure formation. We use the CUBEP^{3}M code which was developed from the PMFAST code (Merz et al. 2005; see Iliev et al. 2008a for a short description of the CUBEP^{3}M code). It uses particle–particle interactions at subgrid distances and a particle-mesh method for

larger distances. Here, we use the results of two simulations, performed with CUBEP^{3}M, one for a volume of 163 Mpc on a side and the other with 53 Mpc. The former has 3072^3 particles and a mesh size of 6144^3 cells, while the latter has 1024^3 particles and 2048^3 cells, which imply particle masses of 5.5×10^6 and 5.1×10^6 $M_\odot$, respectively. These parameters guarantee a minimum resolved halo mass of 10^8 $M_\odot$ which is approximately the minimum mass of haloes able to cool by atomic hydrogen cooling. The cosmological parameters used were for a flat ΛCDM universe with $\Omega_m = 0.27$, $\Omega_b = 0.044$, $h = 0.7$, $n = 0.96$ and $\sigma_8 = 0.8$, based on the 5-yr *WMAP* results (Komatsu et al. 2009).

2.2 Radiative transfer runs

Table 1 gives an overview of the seven different radiative transfer runs that we analyse in this paper. These are a subset of a larger suite of simulations, to be presented in a follow-up paper (Iliev et al., in preparation). This subset was chosen as the minimum one needed to illustrate the points we want to make in this work. All the radiative transfer simulations were performed using the C^2-RAY method (Mellema et al. 2006b) on a uniform rectilinear grid containing 256^3 grid cells. The density is assigned to the mesh by smoothing the dark matter particle distribution from the underlying *N*-body simulation using an smoothed particle hydrodynamics kernel function: each *N*-body particle is assigned a compact, spherical smoothing kernel whose width is adjusted so as to encompass its 32 nearest neighbours. Particle mass is then assigned to the cells of our radiative transfer grid by integrating each kernel function over the volume of each cell it overlaps. To convert what is the IGM dark matter density into a baryon density, we assume that in the IGM the gas distribution follows the dark matter. This is valid on the scales of the radiative transfer cells (0.2 or 0.6 comoving Mpc) as at the mean density of the IGM they are much larger than the local Jeans length.

There are physical effects below our resolution limit which influence reionization. These are small-scale density variations ('clumping') and the presence of unresolved absorbers (such as minihaloes and the structures of unknown origin which are observed as Lyman-limit systems at lower redshifts). All of these will slow down the reionization process as they increase the number of photons absorbed. In the simulations presented here, we do not consider these effects (but see e.g. Ciardi et al. 2006; McQuinn et al. 2007; Alvarez & Abel 2010; Crociani et al. 2011, for studies about the effect of different types of unresolved absorbers; Iliev et al. 2006b; McQuinn et al. 2007; Iliev et al. 2008b, for compartative studies of the effect of clumping).

Simulations are labelled with the parameter g_γ, which is an efficiency factor for the ionizing photon production of haloes per source halo baryon per unit time. Each halo of mass M is assigned a luminosity

$$\dot{N}_\gamma = g_\gamma \frac{M\Omega_b}{10\mu\Omega_0 m_p}, \quad (1)$$

where $\dot{N}_\gamma$ is the number of ionizing photons emitted per Myr, M is the halo mass and m_p is the proton mass. Haloes are assigned different luminosities according to whether their mass is above ('large sources') or below ('small sources') 10^9 $M_\odot$ (but above 10^8 $M_\odot$). For example, 53Mpc_g8.7_130S indicates that large sources have an efficiency $g_\gamma = 8.7$, while small sources have an efficiency $g_\gamma = 130$, and the symbol 'S' means that the small sources are suppressed in regions where the ionization fraction is higher than 10 per cent.

In previous simulations performed with C^2-RAY, the source efficiencies were characterized by f_γ, the number of ionizing photons released per source halo baryon per star-forming episode (i.e. per simulation time-step for updating the source halo catalogue from the *N*-body results). The relation between f_γ and g_γ is given by

$$g_\gamma = f_\gamma \left(\frac{10\ \mathrm{Myr}}{\Delta t}\right), \quad (2)$$

where Δt is the time between two snapshots from the *N*-body simulation. For example, Iliev et al. (2008b) considered a simulation called f250. In the new naming scheme, this would be called g112. The reason for switching to the new naming scheme is that the previous scheme hid the dependence on the size of the time-step Δt, since f_γ ionizing photons were released over a time Δt per baryon for all the baryons inside source haloes when that step began. This made it more difficult to compare simulations involving different time-steps, since the results depend on both f_γ and Δt, while the instantaneous luminosities of source haloes depend only upon their ratio $f_\gamma/\Delta t$, not f_γ alone.

The suite of simulations presented in Table 1 allow us to see how the morphology and characteristic scales of reionization depend upon various important numerical and physical parameters which

Table 1. Simulation parameters, volumes derived from this and global (mass-averaged) reionization history results for simulations with *WMAP*5 cosmology parameters. The box sizes can be directly inferred from the simulation names. For all simulations, the mesh consists of 256^3 cells. The ionization time-step for all simulations is $\Delta t_i = 5.75 \times 10^6$ yr. g_γ is the efficiency parameter as explained in the text; the old efficiency paramter f_γ is given in brackets; V_{min} is the comoving volume of the minimum-size H II region, ionized by the least-efficient source during one time-step, assuming the density to be the average density of the universe; and τ_{es} is the electron scattering optical depth calculated for each simulation.

	53Mpc_g8.7_130S	163Mpc_g8.7_130S	53Mpc_g8.7_130	53Mpc_g1.7_8.7S	53Mpc_g0.4_5.3	53Mpc_uvS_1e9	53Mpc_g10.4_0
$^{high}_{mass}$ g_γ (f_γ)	8.7 (10)	8.7 (10)	8.7 (10)	1.7 (2)	0.4 (0.4)	Variable → Fig. 1	10.4 (12)
$^{low}_{mass}$ g_γ (f_γ)	130 (150)	130 (150)	130 (150)	8.7 (10)	5.3 (6)	0 (0)	0 (0)
Suppression	Yes	Yes	No	Yes	No	n/a	n/a
V_{cell} (Mpc^{-3})	0.0088	0.2575	0.0088	0.0088	0.0088	0.0088	0.0088
V_{min} (Mpc^{-3})	0.1361	0.1361	0.1361	0.0136	0.0084	>0.1361	0.1627
$z_{10\,per\,cent}$	13.6	13.3	15.8	10.1	11.7	13.7	10.5
$z_{30\,per\,cent}$	10.6	10.4	14.6	8.5	10.3	10.6	9.6
$z_{50\,per\,cent}$	9.7	9.4	14.0	7.7	9.7	9.7	9.1
$z_{70\,per\,cent}$	9.2	8.9	13.6	7.3	9.3	9.3	8.8
$z_{99\,per\,cent} = z_{ov}$	8.6	8.3	13.0	6.7	8.6	8.5	8.3
τ_{es}	0.083	0.080	0.13	0.058	0.078	0.084	0.071

are not yet well understood. Simulation 53Mpc_g8.7_130S is our standard case for this paper. We refer to this as the fiducial simulation. It produces an electron scattering optical depth consistent with the 1σ range allowed by the 7-yr *WMAP* results, $\tau_{\rm es} = 0.088 \pm 0.015$ (Komatsu et al. 2011). To test the effect of weaker sources and thus more extended reionization, we also present 53Mpc_g1.7_8.7, which ends considerably later and has an optical depth consistent with the 7-yr *WMAP* results when considering the 2σ range (and assuming a Gaussian error distribution) for $\tau_{\rm es}$. These two simulations are used to introduce the different analysis methods in Section 3.

One of the physical effects which may be present during reionization and which we study in this paper is source suppression due to Jeans mass filtering, in which ionizing radiation from sources hosted by haloes with a mass below some threshold is suppressed when the haloes are located within ionized regions (e.g. Shapiro, Giroux & Babul 1994). This concept was introduced in our simulation models in Iliev et al. (2007). By comparing, for example, 53Mpc_g8.7_130S to 53Mpc_g8.7_130 (the latter without source suppression), it is possible to isolate the effects due solely to source suppression. However, the simulation with no suppression will end at a much higher redshift and therefore the halo populations are not comparable at corresponding stages of reionization (e.g. at $z_{50\,\rm per\,cent}$). Hence, we also include simulation 53Mpc_g0.4_5.3 which does not have suppression, but which, due to the weaker source luminosities, ends approximately at the same time as our fiducial simulation 53Mpc_g8.7_130S. This way the different reionization stages (except the earliest ones) occur at similar times, and thus these two simulations have similar halo populations at the different stages of reionization.

For the 54-Mpc simulation volume at $z \sim 13.6$, there are roughly 330 cells containing source haloes more massive than $10^9\,{\rm M}_\odot$ (this corresponds to roughly 2×10^{-3} per cent of all cells). Additionally, there are about 38 000 cells (2.5×10^{-1} per cent) containing low-mass source haloes between 10^8 and $10^9\,{\rm M}_\odot$. However, for the fiducial simulation, for example, roughly 88 per cent of these low-mass source haloes are suppressed. For the large simulation volume, these numbers (also at roughly 10 per cent of the global ionization fraction i.e. $z \sim 13.2$) are: 12 000 cells containing massive haloes (7.8×10^{-2} per cent of all cells) and 750 000 cells (4.8 per cent of all cells) containing low-mass haloes, of which roughly 86 per cent are suppressed. At overlap, the small (large) simulation volume has about 17 000 (440 000) cells containing massive source haloes, which corresponds to 0.1 (2.8) per cent of all cells. The number for low-mass haloes is 280 000 (3600 000) cells or 1.8 (13) per cent of all cells, almost all are completely suppressed.

Throughout this study, we will make comparisons like indicated above for the case of source suppression, in order to see how physical effects manifest themselves and to find which quantitative measurements best discriminate among different reionization scenarios. Instead of comparing the simulations at equal redshifts, we do the comparison at equal mass averaged (global) ionization fraction, $\langle x \rangle$. Table 1 lists the redshifts at which the global ionization fraction (i.e. mass-weighted average, unless otherwise stated) for each simulation is $\langle x \rangle \sim 0.1$, 0.3, 0.5, 0.7 and 0.99. The epoch at which the H II regions globally 'overlap', $z_{\rm ov}$, will, by convention, be taken here to be the redshift at which $\langle x \rangle = 0.99$, although the value of $z_{\rm ov}$ which results is not very sensitive to this particular choice as long as $\langle x \rangle$ is close to unity.

Besides the above-mentioned simulations, there are three more simulations included in this study: the simulation labelled 53Mpc_uvS_1e9 has the same (imposed) global photon production history as our fiducial simulation, but only haloes more massive than $10^9\,{\rm M}_\odot$ are allowed to host luminous sources. This results in a g_γ that is time-dependent. Its evolution is plotted in Fig. 1 as a function of time and mass-averaged ionization fraction $\langle x \rangle$.

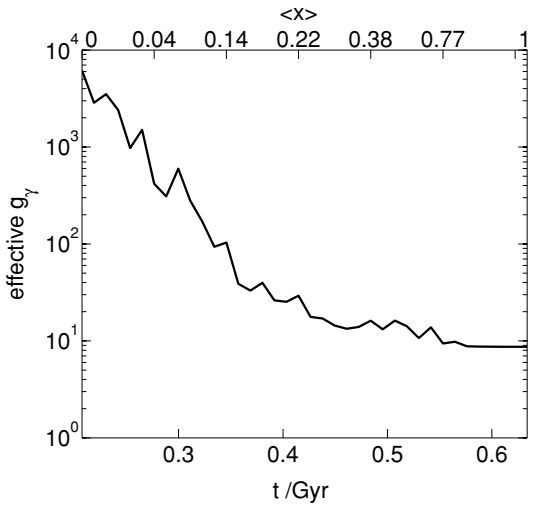

Figure 1. Evolution of the effective efficiency factor g_γ for the simulation with imposed photon production history (53Mpc_uvS_1e9) as a function of time and global ionization fraction.

As a second simulation with only high-mass sources, we include simulation 53Mpc_g10.4_0. Unlike 53Mpc_uvS_1e9, it has a constant mass-to-light ratio which is chosen so that reionization ends roughly at the same time as in our fiducial simulation. This yields later $z_{10\,\rm per\,cent} - z_{70\,\rm per\,cent}$ and thus a lower value of $\tau_{\rm es}$. Note that the efficiency of sources in high-mass haloes had to be boosted only by a factor of 1.2. This means that in our fiducial simulation, sources in low-mass haloes only contribute about 17 per cent to the ionizing photon budget.

Simulation 163Mpc_g8.7_130S has the same physical parameters and the same mass resolution and, hence, halo mass range as our fiducial simulation, but the simulation box volume is about 30 times bigger. Therefore, it is capable of catching structure on larger scales. On the other hand, the resolution in the radiative transfer simulation is worse than in the small box simulation since the number of cells in both simulations is 256 per side. This simulation is included to check for cosmic-variance effects and to test the effect of resolution on our investigation methods.

Snapshots of the simulations at the 30 per cent global (mass-averaged) ionized fraction are shown in Fig. 2. The slices are to the same comoving physical scale to make it more easy to see the morphological and topological differences between the models which we will discuss in detail below.

Table 1 also lists values for the smallest possible H II region, $V_{\rm min}$, which could be formed during a single radiative transfer time-step Δt_i if the surrounding IGM has the average density of the universe and recombinations can be neglected. This number is likely to be an overestimate as recombinations and density peaks will reduce it. However, it is a useful number to compare the resolution of various radiative transfer simulations with. The number of emitted ionizing photons from the smallest haloes of mass $M_{\rm min}$ is given by

$$N_{\rm min} = \dot{N}_\gamma \Delta t_i = \frac{g_\gamma}{10} \frac{M_{\rm min}\Omega_{\rm b}}{\mu m_{\rm p}\Omega_0} \frac{\Delta t_i}{\rm Myr}\,, \qquad (3)$$

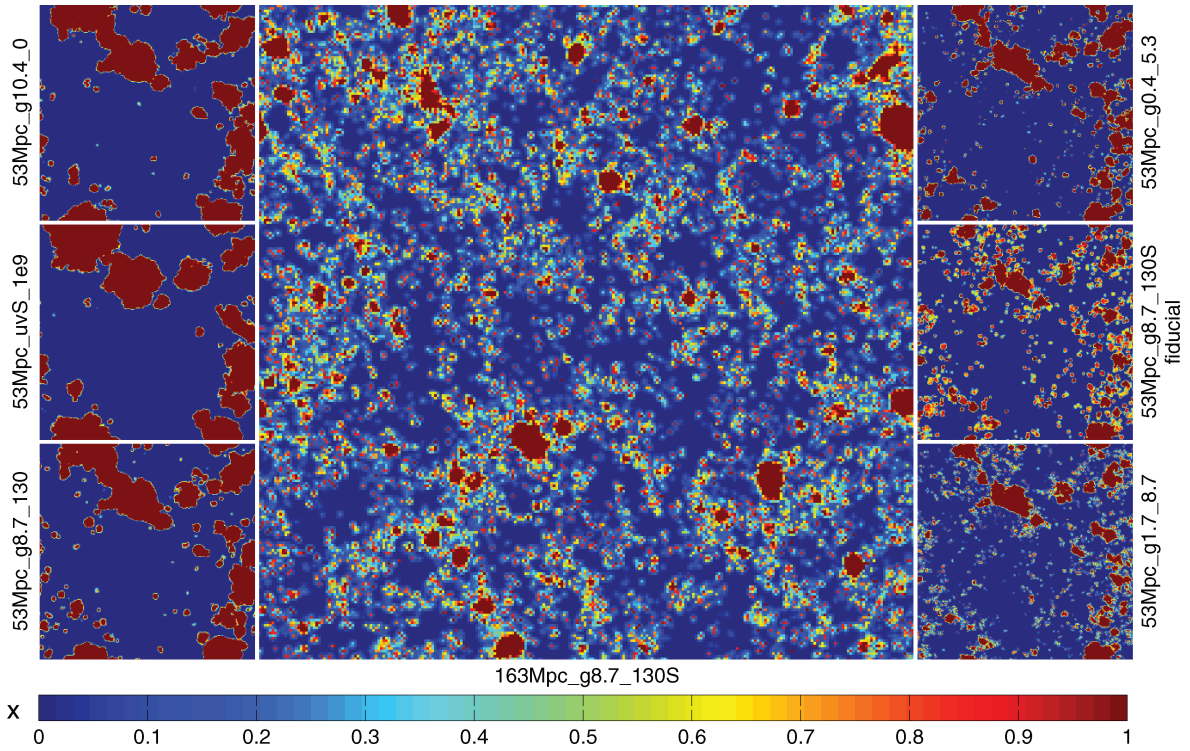

Figure 2. Ionization maps (ionization fraction according to colour bar) of all included simulations at 30 per cent global ionized fraction: from the top left-hand side to bottom right-hand side: 53Mpc_g10.4_0, 53Mpc_uvS_1e9, 53Mpc_g8.7_130, 163Mpc_g8.7_130S, 53Mpc_g0.4_5.3, 53Mpc_g8.7_130S and 53Mpc_g1.7_8.7S. Each panel is for a slice which is one cell thick (∼0.64 and ∼0.21 Mpc, respectively, for the 163- and 53-Mpc simulations).

which then gives a minimum volume of

$$V_{\rm min} = \frac{N_{\rm min}}{n_{\rm H}} = \frac{g_\gamma M_{\rm min}}{\Omega_0 \rho_{\rm crit,0}} \frac{\Delta t_i}{10\,{\rm Myr}} \simeq 0.0016\,{\rm Mpc}^3 \left(\frac{M_{\rm min}}{10^8\,{\rm M}_\odot}\right) g_\gamma\,, \quad (4)$$

where we have used the radiative transfer time-step $\Delta t_i = 5.75 \times 10^6$ yr and $n_{\rm H} = \frac{\rho_{\rm crit,0}}{\mu m_{\rm p}} \Omega_{\rm b}$ is the hydrogen number density. $V_{\rm min}$ can be compared to the cell sizes of the simulations which are also listed in Table 1.

3 INTRODUCING THE ANALYSIS METHODS

In this section, we introduce our analysis methods by means of two simulations that differ only in the mass-to-light ratio of the haloes, 53Mpc_g8.7_130S and 53Mpc_g1.7_8.7S. Whenever we refer to 'the simulations' in this section, we mean these two. The focus in this section is on the ability of our analysis methods to discriminate between the two simulations. The results of all methods together can be seen as a characterization of the morphology of the ionization fraction.

3.1 Size distribution

One of the most basic measures of reionization is the size distribution of H II regions. However, as will become clear below, the 'size of an H II region' is a quantity which can be defined in different ways. Under the assumption that most of the volume is either highly ionized or highly neutral, H II regions can be considered to be topologically connected volumes of space. We previously used a friends-of-friends (FoF) method (Iliev et al. 2006b) to identify such regions, using the condition $x > 0.5$ for a cell to be considered ionized. In contrast to this measure of the volume of connected ionized space, Zahn et al. (2007) used a different method, introduced as 'the bubble probability distribution'. For reasons we explain below, we refer to this method as the 'spherical average' (SPA) method. We now describe these two methods in more detail.

3.1.1 *Friends-of-friends method*

Our first method for identifying the size distribution of H II regions relies on a literal definition of 'H II region': a connected region in which hydrogen is mostly ionized. For grid data, the obvious way to identify such a connected region is to use a 'FoF' approach, in which two neighbouring cells are considered friends if they both fulfill the same condition. Cells are grouped into distinct regions according to whether they are linked together in an extended network of mutual friends. The algorithm we use to group cells together is the equivalence class method, described in Press et al. (1992). Unless otherwise specified, we use $x > 0.5$ for a cell to be considered ionized and $x \leq 0.5$ for a cell to be considered neutral, so that every point in the simulation box is either in an H I or in an H II region. Our method was first described in Iliev et al. (2006b). In contrast to all other size measures presented below, the FoF does not care about how contorted an H II region is. Therefore, the sizes of H II regions found by the FoF method and the sizes of H II regions found by other methods, which will be introduced below, give complementary information about the morphology of the ionization fraction field.

The FoF method has been used extensively for halo finding in cosmological N-body simulations (Davis et al. 1985). Our implementation is more straightforward, since each cell always has only

six direct neighbours, the identities of which are known in advance, as opposed to particle data, in which it is necessary to perform costly searches to identify the groups. Another significant difference between the two methods is the role played by free parameters. In the halo finding FoF method, the free parameter is the linking length, which is the distance within which two particles are considered to be friends. In the region-finding method, the free parameter is the threshold, $x_{\rm th}$, for a cell to be considered ionized or neutral.

As seen in Fig. 3, we test the effect of varying $x_{\rm th}$ (using our fiducial simulation 53Mpc_g8.7_130S at 50 per cent global ionization fraction), where we used three different values for $x_{\rm th} = 0.1$, 0.5 and 0.9. The thin dot–dashed black line shows at every volume V, how much a single region with this volume would contribute. This means that each bin cannot be filled less (i.e. or the bin must be empty) than to the point where this line crosses the lower limit of each volume bin.

As can be inferred from Table 1, the minimum volume ionized by a source in a single radiative transfer time-step for our fiducial simulation is about an order of magnitude bigger than the cell size. This means that at the end of the radiative transfer time-step at which the source turned on, the cell hosting the halo will be completely ionized and surrounded by partly ionized cells. If regions are connected through such partly ionized border cells, it strongly depends on $x_{\rm th}$ if the regions count as two disconnected or as one connected region. In every analysis method that depends on a threshold value, this effect is bigger if the partly ionized borders of ionization regions are comparable to the regions' size. Nevertheless, as can be seen in Fig. 3, the qualitative picture remains unchanged, with a few cell regions, a substantial contribution of regions of intermediate size and the main contribution coming from a single large region comparable in size to the simulation box. The absence of single-cell regions for $x_{\rm th} = 0.1$ can be explained by looking at the minimum number of photons from a single source released during one time-step. Sufficient photons are produced to ionize the cells surrounding the source cell more than 10 per cent, even if the density of the cells is nine times the average density of the universe (see equation 4).

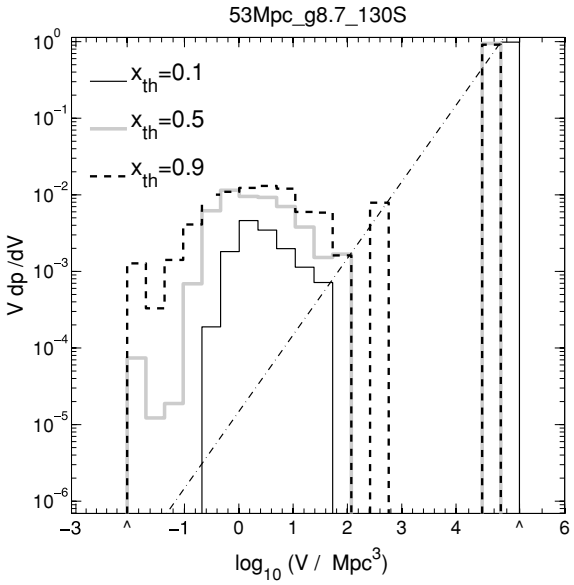

Figure 3. Effect of varying the threshold $x_{\rm th}$ for the FoF method for the 53Mpc_g8.7_130 simulation at $z = 9.7$, when the global ionized fraction $\langle x \rangle$ is about 50 per cent. The results for three different threshold limits are shown, as indicated in the figure. The thin dot–dashed black line shows at every volume V, how much a single region with this volume would contribute. Indicated by ^ on the abscissa are the cell and box volume.

Below, we convert the volume bins into equivalent radius bins, $R_{\rm equi,FoF} = [3/(4\pi)V]^{(1/3)}$ which corresponds to the radius $R_{\rm equi,FoF}$ of a spherical region with the same volume. We want to stress that this does not mean that the H II regions are spherical. We convert to an equivalent radius only to allow a more direct comparison to the SPA method and the PS which are described in the following sections. We normalize to the total volume and not to ionized volume, to allow for a more direct comparison to the PS which is normalized in the same way.

In order to show the time-evolution of the FoF size distribution of ionized regions for a simulation in a single plot, we choose a fixed threshold value ($x_{\rm th} = 0.5$) and colour code the contribution $V{\rm d}p/{\rm d}V$. The colour coding makes it possible to show a histogram (like Fig. 3) in a single line or column. Each individual column of Fig. 4 (left-hand panel) is a histogram as Fig. 3 at a different global ionization fraction. Fig. 4 thus shows the evolution of the size distribution with global ionization fraction. The box and the cell size are marked with > on the ordinate. By construction the FoF method will not result in sizes larger than the former and smaller than the latter. As we will see later, H II regions start to merge very early on in the course of reionization which results in shapes far from spherical and a complex topology already at global ionization fractions $\langle x \rangle \sim 0.2$. The concept of distinct H II regions and their sizes quickly becomes meaningless. Therefore, all size distribution estimates are only shown up to a global ionization fraction $\langle x \rangle \sim 0.6$.

Three things catch the eye when analysing the size evolution in Fig. 4:

(1) Already at $\langle x \rangle \sim 0.15$, the distribution for both simulations is not continuous, but shows a gap. Most of the ionized volume is contained within one region of a size falling into a size bin which is separated from the rest. This is an inherent property of the FoF method, where regions are grouped together as soon as they touch and the local H II region percolation occurs quite early in the evolution. If the H II regions reach a certain size, which depends on the clustering of the sources and on their efficiency, they will percolate and form bigger H II regions. As those smaller H II regions grow and merge into the larger one, both their numbers and the fraction of the ionized volume that they occupy decrease. A doubling of the volume (merging of two bubbles with the same

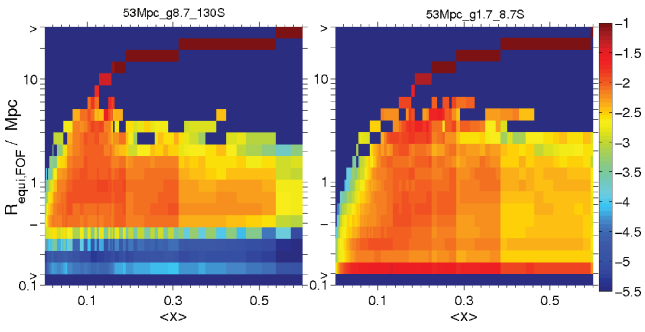

Figure 4. Size distributions using the FoF method for simulation 53Mpc_g8.7_130S (53Mpc_g1.7_8.7S) in the left-hand (right-hand) panel as a function of the global ionization fraction $\langle x \rangle$. $V{\rm d}p/{\rm d}V$ is colour coded according to the colour bar. The equivalent radii corresponding to the cell and box volume of the 53 Mpc box, $R_{\rm equi,FoF} = 0.13$ and 32.8 Mpc, respectively, are marked by >. Additionally, the cell size for the 163-Mpc simulations, $R_{\rm equi,FoF} = 0.4$ Mpc (see Section 4) is indicated by -.

size) thus corresponds to a jump over one effective radius bin. The largest H II region grows through mergers with smaller H II regions, as well as due to sources within the region, and approaches the box size by $\langle x \rangle \sim 0.6$.

(2) The distribution of the smaller scales (i.e. everything except the one big region) is much flatter for simulation 53Mpc_g1.7_8.7S. This simulation has more single- or few-cell-sized regions than our fiducial simulation 53_Mpc_g8.7_130S.

(3) While the size bin which contributes most to the global ionization fraction is increasing with $\langle x \rangle$, the shape of the distribution of the rest does not change much. However, its total contribution to the global ionization fraction decreases with $\langle x \rangle$: at the same rate that small H II regions grow bigger and merge into even bigger H II regions, new small ones are 'born' but contribute in the course of reionization less and less to the global ionized fraction.

The FoF method applied to an ionization field in a finite simulation box can only sample the true underlying size distribution function (as it would be in an infinite simulation box) up to a lower limit. This is indicated by the thin dot–dashed black line in Fig. 3. This lower limit depends on the size of the simulation box. The better the sampling (i.e. the bigger the simulation box) the smaller the gap mentioned above.

3.1.2 *Spherical average method*

The SPA method was described by Zahn et al. (2007); it can be easily used for comparisons with analytical models. It is based on constructing spheres around every cell in the computational volume, averaging the ionization fraction inside these spheres and finding the largest such sphere for which the average ionization fraction is greater than a certain threshold $x_{\rm th}$. We chose $x_{\rm th} = 0.9$. Because of this, we call it the *SPA* method. It yields a smoother distribution of H II region sizes than the one obtained by the FoF method. It does not measure the size of a connected ionized space, but instead it is a measure of the scales of spherical bubbles which would cover the ionized space.

Motivated by the analysis given in Appendix A, we multiply the radius found by the SPA method by a factor of 4, $s = 4 \times R$. We call this the scale of the SPA method. In Fig. 5, we plot the SPA distribution in the same way as the FoF distribution in Fig. 4. $R{\rm d}P/{\rm d}R$ is normalized to the whole volume. We define $R_{\rm max}(\langle x \rangle)$ to be the position of the maximum of $R{\rm d}P/{\rm d}R$ at every $\langle x \rangle$. We see that $R_{\rm max}$ is increasing with $\langle x \rangle$ which means an increase in the average bubble size with global ionization fraction, as expected. Although initially smaller, it can be seen that the average scale of simulation 53Mpc_g1.7_8.7S is growing faster with respect to $\langle x \rangle$ than the average scale of simulation 53Mpc_g8.7_130S. From Fig. 5, it can be further seen that the distribution of the model with the smaller efficiencies shows initially (at $\langle x \rangle \lesssim 0.1$) a wider distribution of bubble sizes with a peak at smaller scales: the smallest H II regions are smaller than in the fiducial model, but the contribution from small regions to the total ionized fraction is smaller. Therefore, the bigger H II regions have to grow to a bigger size in the 53Mpc_g1.7_8.7 model to reach an ionization fraction of 10 per cent. At higher average ionization fractions, the peak of the distribution is slightly shifted towards bigger scales with respect to the 53Mpc_g8.7_130S model.

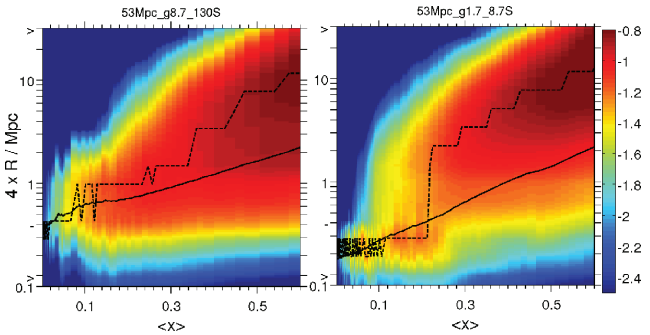

Figure 5. Size distributions using the SPA method as explained in the text, $\log_{10} R{\rm d}P/{\rm d}R$ colour coded according to colour bar; left-hand (right-hand) panel simulation 53Mpc_g8.7_130S (53Mpc_g1.7_8.7S) as a function of the global ionization fraction $\langle x \rangle$. The peaks of the distribution at every global ionization fraction are indicated by the dashed line. The black solid line shows the $3V/A$ size measure, as explained in Section 3.1.3.

As we have already noted, much of the notable difference in the FoF curves comes from a very small fraction of the volume and a log scale is required to see such differences in the FoF plots. The SPA distributions are much smoother and therefore offer a less-detailed, more global picture of the spatial structure of the ionized regions. However, the SPA shows much more clearly the difference in the size of the large-scale H II regions between the two simulations.

Another method which is similar to the SPA method is a method used in Mesinger & Furlanetto (2007). We examine this method in Appendix B. We find that it yields qualitatively the same results as the SPA and PS, but its use in simulations with a continuous distribution of ionization fractions (i.e. not a binary field) creates complications.

3.1.3 *3V/A method*

As another estimate of the scale of bubbles, one could use the ratio of the total volume of the H II regions and their total surface area:

$$3 \times \sum_{\text{H II regions}} \text{Volume} \Big/ \sum_{\text{H II regions}} \text{Area}. \qquad (5)$$

The volume V and the surface area A were calculated from the zeroth and first Minkowski functionals, respectively: $V = V_0$ and $A = 6 \times V_1$. For a distribution of disconnected spherical bubbles, $3V/A$ is the surface weighed average radius. For three-dimensional bodies, one could say that $3V/A$ is proportional to the surface weighted average of the smallest scale of each object. If the dominant structures are two-dimensional, that is, disc-like, then $3V/A$ is three times bigger than the surface weighted average disc height. If the dominant structure is one-dimensional, that is, bar-like, $3V/A$ is 1.5 times the surface weighted average bar radius. In any case, in terms of surface weighted averages, it is an overestimate of the minimum scales. As in the case of the SPA method, $3V/A$ does not measure the sizes of topologically connected ionized volumes.

It can be seen (Fig. 5) that initially, for both simulations, the $3V/A$ scale agrees with the scale of the maxima of the SPA. At about 20 per cent global ionization fraction, the scale of the maxima of the SPA for the 53Mpc_g1.7_8.7S simulation is greater than the scale estimated by $3V/A$, indicating that while most of the volume is contained in larger scale bubbles, most of the surface comes from small-scale bubbles: many very small scale structures and few very large scale structures. For the fiducial simulation, the offset between the scale of the maximum of the SPA and the scale estimated by $3V/A$ is smaller, indicating that the same bubbles which contribute substantially to the total volume contribute substantially to the total surface area.

3.2 Power spectra

The typical reionization scales can be further characterized by the appearance of features in the power spectra of the density and ionized fraction fields, $P_{\delta\delta}$, $P_{x\delta}$ and P_{xx}, where $\langle\delta_{\boldsymbol{k}}\delta^*_{\boldsymbol{k}'}\rangle \equiv (2\pi)^3\delta^3(\boldsymbol{k}-\boldsymbol{k}')P_{\delta\delta}(k)$, $\langle\delta_{x\boldsymbol{k}}\delta^*_{\boldsymbol{k}'}\rangle \equiv \delta^3(\boldsymbol{k}-\boldsymbol{k}')(2\pi)^3P_{x\delta}(k)$ and $\langle\delta_{x\boldsymbol{k}}\delta^*_{x\boldsymbol{k}'}\rangle \equiv \delta^3(\boldsymbol{k}-\boldsymbol{k}')(2\pi)^3P_{xx}(k)$. Here, δ is the overdensity of matter, while $\delta_x \equiv x - x_{\rm v}$, where $x_{\rm v}$ is the volume-weighted global average ionized fraction. Note that we do not normalize δ_x by $x_{\rm v}$. When plotting the actual PS, we use the dimensionless power per logarithmic interval in wavenumber, $\Delta^2(k) \equiv k^3P(k)/(2\pi^2)$.

The PS of the ionization fraction field is one component in the expansion of the neutral hydrogen PS (e.g. Furlanetto, Oh & Briggs 2006). As pointed out in Section 1, future 21-cm radio observations aim at observing this quantity via the 21-cm line of neutral hydrogen. Therefore, from all methods presented here to characterize the morphology of the ionization fraction field, the PS of the ionization fraction is the measure most closely related to observations.

Shown in Fig. 6 is the ionized fraction PS, $\Delta^2_{xx}(k)$, for the two simulations as a function of global ionization fraction on the abscissa. Instead of plotting $\Delta^2(k) \equiv k^3P(k)/(2\pi^2)$ against k, we choose to plot it against $2.46/k$, the reason for this will become clear later. This colour contour plot thus shows the evolution of $\Delta_{xx}(k)$ during reionization. For the 53Mpc_g8.7_130S model, it can be seen that the PS first peaks at scales of the order of $s = 2.46/k_{\rm max} \sim 0.8$ Mpc. We expect this peak to be associated with the the size of ionized or neutral bubbles, for the following simple reason. On scales smaller than the bubbles, the correlation function $\xi_{xx}(r_{12}) = \langle[x(\boldsymbol{r}_1) - x_{\rm v}][x(\boldsymbol{r}_2) - x_{\rm v}]\rangle$ reduces to the constant value $x_{\rm v}(1 - x_{\rm v})$, while on scales much larger than the bubbles, the ionized fraction is uncorrelated and the correlation function should approach zero (Zaldarriaga et al. 2004). This behaviour for the correlation function implies that the PS $\Delta^2(k)$ should approach zero at large and small scales, with a peak at the characteristic size of the bubbles.

The first peak of $\Delta^2_{xx}(k)$ for a single spherical top-hat bubble of radius s would be located at $k_{\rm max} \approx 2.46/s$, which is why we use $2.46/k_{\rm max}$ to characterize the typical radius of regions. Indeed, comparison of the maxima of the SPA model and the peaks of the power spectra shows that they are approximately related by $2.5/k_{\rm max} \sim 4R_{\rm max}$ as can be seen by comparing Figs 5 and 6. It should be noted that both, the SPA and the PS, do not show a pronounced peak at all global ionization fractions, but are instead flat at higher global ionization fractions. This is in agreement with

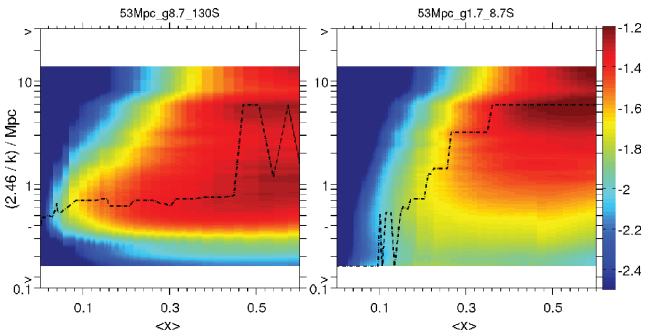

Figure 6. Power spectra of ionized fraction as a function of global ionization fraction, $\Delta^2_{xx}(k)$ colour coded according to the colour bar; left-hand (right-hand) panel for the fiducial simulation 53Mpc_g8.7_130S (53Mpc_g1.7_8.7S). The dashed line indicates the peak of $\delta^2_{xx}(k)$ as a function of $\langle x\rangle$. Note that $\Delta^2(k)$ is plotted over a multiple of inverse k; for details, see text.

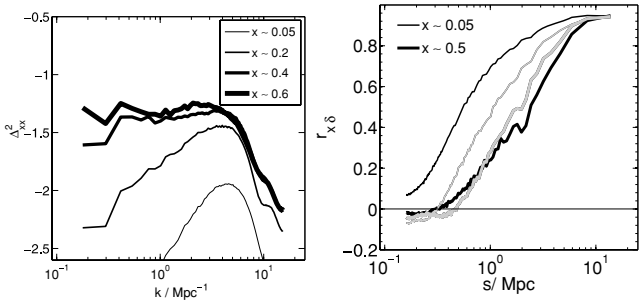

Figure 7. Left-hand panel: PS of the fiducial simulation at several different global ionization fractions as indicated in the legend. Right-hand panel: cross-correlation coefficient $r_{x\delta}$ as defined in equation (6) as a function of $2.46/k$ at $\langle x\rangle = 0.05$ and 0.5 [as indicated in the figure (by line thickness) for the fiducial simulation (grey lines) and 53Mpc_g1.7_8.7S (black lines)]. Note the lower correlation between the ionized fraction and density for the fiducial simulation on all scales at low global ionization fractions.

one of the trends that Zahn et al. (2010) identify for all their tested reionization models. To better show this behaviour of the PS at higher global ionization fractions, we show the PS of the fiducial simulation as a function of k for four different global ionization fractions as a line-plot in the left-hand panel of Fig. 7. However, the other trend they identify, the shift towards smaller k with increasing lower ionization fraction is less apparent for our fiducial simulation. Instead, the form of the PS of the fiducial simulation suggests that at a global ionization fraction greater than $\langle x\rangle \sim 0.4$ there are two main populations of bubbles: one at sizes where the PS initially peaks, around 0.8 Mpc, and the other with sizes around 6 Mpc, which is of the size of clusters of galaxies, that is, the typical clustering scale of the source haloes at this epoch, not to be confused with the length-scale which encompasses the mass of the higher mass, virialized galaxy clusters familiar at lower redshift. The first scale results from the suppression of sources after initial turn-on of a source in a low-mass halo. Growth of the H II region is completely halted until a high-mass halo forms in that region. A less-stringent suppression criterion would slow down the growth, but probably not halt it entirely. The second scale results from merging of bubbles emerging from galaxies in the same cluster. These details in the size distribution are washed out in the SPA distribution. However, it should be noted that a scale of 6 Mpc is a substantial fraction of a 53-Mpc box and therefore it is questionable if the sampling at this scale is high enough. At global ionization fractions larger than $\langle x\rangle \sim 0.4$, it can be seen that there is considerable power on scales comparable to the box size.

For the 53Mpc_g1.7_8.7S simulation, it can be seen that there is more power on smaller scales, but also that the PS is flatter than the one of the fiducial model as there is no distinct peak below global ionization fractions of 20 per cent. Further it can be seen that the slope of isochromatic lines is greater for this model than for the fiducial one. This means that the sizes of H II regions in the 53Mpc_g1.7_8.7S simulation are growing faster with respect to the global ionization fraction. This was also seen in the SPA results. The absence of the peak at smaller scales that is present in the fiducial model is due to the fact that already at a global ionization fraction of roughly 10 per cent, the contribution from sources hosted by massive haloes is about the same as the contribution from sources in low-mass haloes, while this is true at about 70 per cent global ionized fraction for our fiducial simulation. Therefore, the relative contribution from H II regions produced by sources in low-mass haloes in isolated cells is smaller. H II regions produced by

sources in massive haloes will grow continuously, explaining the flat distribution below several Mpc.

The right-hand panel of Fig. 7 shows the cross-correlation coefficient of ionized fraction and density field:

$$r_{x\delta}(k) \equiv \frac{\Delta^2_{x\delta}(k)}{\left[\Delta^2_{xx}(k)\Delta^2_{\delta\delta}(k)\right]^{1/2}} \tag{6}$$

at two different $\langle x \rangle \sim 0.05$ and 0.5 for both simulations plotted against $s = 2.46/k$. When $r_{x\delta} = (-1)1$, the ionized fraction and density field are perfectly (anti-)correlated, while $r_{x\delta} = 0$ implies they are uncorrelated. As seen from the figure, the ionized fraction and density fields are nearly perfectly correlated on large scales, $s \gtrsim 8$ Mpc. It can be seen that the scale s at which the correlation starts to decrease is increasing with global ionization fraction. This is due to the fact that while the H II regions grow, they also start ionizing the voids. At very low global ionization fractions, represented here by $\langle x \rangle \sim 0.05$, the correlation coefficient for simulation 53Mpc_g1.7_8.7S is greater than the one for the fiducial simulation (especially at smaller s). This is expected because the ionizing radiation of the sources in the simulation with lower efficiencies can less easily 'break out' of high-density regions. Additionally, less-efficient sources trace the high-density regions better since clustered low-mass sources are less suppressed: individually, they form smaller H II regions and therefore do not suppress each other. At later stages of reionization, this difference disappears: the simulation with low source efficiencies reaches the same global ionization fraction as the fiducial simulation at much later times when massive sources are more common. Those massive sources form bigger H II regions which also grow into the voids.

3.3 Topology of reionization

Minkowski functionals have been used extensively in cosmology to characterize the topology of large-scale structure (Gott, Dickinson & Melott 1986; Mecke, Buchert & Wagner 1994; Schmalzing & Buchert 1997) and also the non-Gaussianity of the CMB (Komatsu et al. 2009). Recent work has focused on using Minkowski functionals as a way to characterize the morphological structure of reionization (Gleser et al. 2006; Lee et al. 2008).

Both works focused on the topology of the H I density field. They showed the Euler characteristic (or genus, respectively) as a function of neutral density for several different times (i.e. global ionization fractions) and concentrated on the increasing deviations from the typical curve of a Gaussian random field. Here, we will take a complementary approach based upon the topology of the ionization fraction field, rather than the fluctuating neutral density field. Unlike the neutral density field, which takes values spread continuously over a very wide range, the ionized fraction field ranges only between 0 and 1 and, ideally, there would essentially be only two values possible to assign to any given point in space, either 'neutral' values close to zero or 'ionized' values close to unity. In that ideal case, the Euler characteristic for the ionized fraction field would only be a function of time (or of the evolving globally averaged ionized fraction) and be largely independent of the choice of ionization fraction threshold.

We follow the definition and notation of Schmalzing, Kerscher & Buchert (1996) and Schmalzing & Buchert (1997). Consider a scalar function $f(\boldsymbol{x})$ defined at each point $\boldsymbol{x} \in \mathbb{R}^3$. The set $F_{\rm th}$ of all points $\boldsymbol{x}$ for which $f(\boldsymbol{x}) > f_{\rm th}$ defines bodies in three-dimensional space. The zeroth Minkowski functional, $V_0(f_{\rm th})$, is simply the volume of those bodies:

$$V_0(f_{\rm th}) = \int_V \Theta[f_{\rm th} - f(\boldsymbol{x})]\mathrm{d}^3\boldsymbol{x}, \tag{7}$$

where Θ is the Heaviside step function. The next three Minkowski functionals are defined as surface integrals over the boundary of the bodies:

$$V_1(f_{\rm th}) = \frac{1}{6}\int_{\partial F_{\rm th}} (\boldsymbol{x})\mathrm{d}^2A\,, \tag{8}$$

$$V_2(f_{\rm th}) = \frac{1}{6\pi}\int_{\partial F_{\rm th}} (\boldsymbol{x})\left(\frac{1}{R_1} + \frac{1}{R_2}\right)\mathrm{d}^2A\,, \tag{9}$$

$$V_3(f_{\rm th}) = \frac{1}{4\pi}\int_{\partial F_{\rm th}} (\boldsymbol{x})\frac{1}{R_1 R_2}\mathrm{d}^2A\,, \tag{10}$$

where R_1 and R_2 are the principal radii of the curvature along the surface $\partial F_{\rm th}$. The first Minkowski functional is proportional to the integrated surface area. This and the zeroth Minkowski functional were used when calculating the size estimator $3V/A$. The Minkowski functional V_3, which is proportional to the integral of the Gaussian curvature over the surface, is also known as the Euler characteristic, and is equal to

#parts − #tunnels + #cavities.

Applied to the ionization fraction field, two disconnected ionized cells would count as two parts, a ring-like ionized region constitutes a tunnel and one part and a neutral cell completely surrounded by ionized cells is a cavity. Table 1 in Schmalzing et al. (1996) gives an overview of different notations for the Minkowski functionals which only differ in constant factors. The better known quantity genus, g (number of complete cuts one can make through the object without dividing it into disconnected parts), is related to the Euler characteristic by the simple relation $g = 1 - V_3$.[6] For example, a torus has $V_3 = 0$, since it has zero total curvature and has one part and one tunnel. A sphere, on the other hand, has $V_3 = 1$, since it has one part and no tunnels, and positive total curvature.

We oversample the ionization fraction fields before calculating the Euler characteristic. We do this to minimize critical connections of H I and H II regions. A critical connection is, for example, an ionized cell which is connected via an edge to another ionized cell in an otherwise neutral neighbourhood. Appendix C explains in more detail the problems that are involved. Important for the following analysis is to note that oversampling reduces ambiguities concerning the connectivity at a given threshold value, but introduces higher dependencies of V_3 on the threshold value.

In the left-hand panel of Fig. 8, we show the evolution of the Euler characteristic V_3 of the ionized fraction as a function of the threshold $x_{\rm th}$ for our (oversampled) fiducial simulation. We choose to normalize V_3 by dividing by the box size to have an easier comparison when dealing with different box sizes. Between threshold values $x_{\rm th} = 0.2$ and 0.6, the evolution of V_3 is largely independent of the actual choice of $x_{\rm th}$: V_3 rises to a maximum value at a mean ionization fraction of about 5 per cent, after which V_3 decreases

[6] This is true if one considers the Euler characteristic of the volume defined by the set of points. Note that others consider the Euler characteristic of the surface of the set of points defining the volume. In this case, the Euler characteristic χ is a factor of 2 greater, resulting in the relation to genus: $\chi = 2(1 - g)$. This is consistent with the relation $\chi(\partial A) = \chi(A)[1 + (-1)^{d-1}]$, where d is the dimension, A a d-dimensional body and ∂A its $d - 1$-dimensional surface (see equation 18 in Mecke et al. 1994).

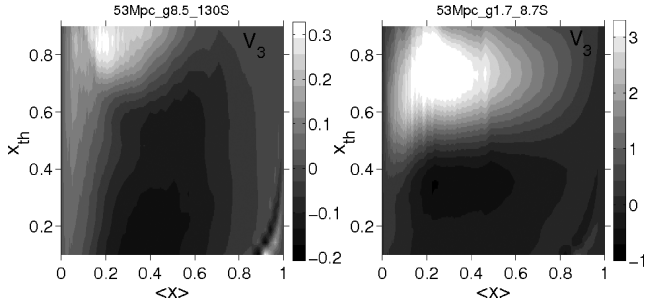

Figure 8. Euler characteristic V_3 as a function of the global ionization fraction $\langle x \rangle$ and threshold value $x_{\rm th}$ for the fiducial simulation (simulation 53Mpc_g1.7_8.7) in the left-hand (right-hand) panel. The fast changes in the lower right-hand corner are due to the implementation of photons that would travel distances longer than the box size (see explanation in the text). Note the high dependence on the threshold value for simulation 38Mpc_g1.7_8.7.

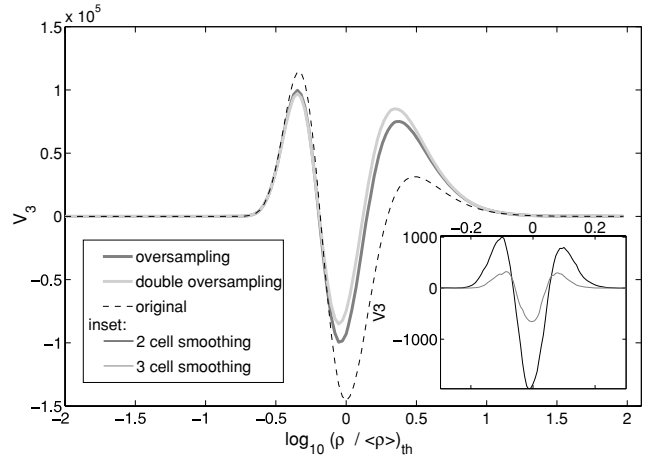

Figure 9. Euler characteristic V_3 of the density field as a function of the density threshold value $\log_{10}(\rho/\langle\rho\rangle$. Shown is V_3 of the original density field at redshift $z = 26.1$ and V_3 of oversampled fields as indicated in the figure. The inset shows V_3 of the smoothed field with two different smoothing widths, as indicated.

and gets negative before 20 per cent global ionization fraction is reached. It rises again after the ionization fraction passed 50 per cent, but never reaches positive values again.

This behaviour can be qualitatively understood by considering inside-out reionization in an approximately Gaussian density field. V_3 for a Gaussian random field (or any monotone and steady function of it) as a function of the threshold value, as plotted, for example, in fig. 1 in Schmalzing & Buchert (1997), shows in the second half a rise to positive values and decreases again. In Fig. 9, we show V_3 of the density field from the 53-Mpc box simulation at redshift $z \sim 26.1$ as a function of the density threshold value.[7] The fact that V_3 of the ionization field does not show a rise to positive values followed by a decrease (see Fig. 8 or Fig. C2) shows that if there exists a monotonic steady functional relation between density and time of ionization, then it does so only until a certain density: low-density areas (the voids in the density field) are ionized 'before their time' and do not serve as positive contributions to V_3 in the ionization field. This is another feature of inside-out reionization: the H II regions do eventually break out in the voids.

It can be seen that V_3 changes very fast at high global ionization fractions, especially when choosing lower threshold values (see the lower right-hand corner in the left-hand panel of Fig. 8). This is due to the way photons that would travel farther than a box distance are implemented in the simulations: the lost photons are collected and evenly distributed over all cells. Cells that only get ionized by those photons have small ionization fractions that only depend on their density.

For very high values of $x_{\rm th}$, the connectivity is reduced; therefore, V_3 is greater due to the positive contribution from many more disconnected H II regions. This reduced connectivity is due to many partly ionized cells originating partly by the relatively small photon output per halo per ionization time-step compared to the average number of atoms in a cell and partly by the oversampling that introduces additional partly ionized cells.

It can be seen (Fig. 8, right-hand panel) that the dependence of V_3 on the threshold value is more pronounced for simulation 53Mpc_g1.7_8.7S. From the FoF investigations (see Fig 4), we know that this simulation has many cell-size H II regions. Also the simple estimates in Table 1 show that the smallest sources are not efficient enough to ionize their own cell, producing partly ionized cells. Therefore, a strong dependence on $x_{\rm th}$ is to be expected. This shows that the resolution for this choice of source efficiencies is not sufficient for doing topological investigations. Due to our choice of oversampling the data, choosing a higher threshold value ($x_{\rm th} \sim 0.5$) corresponds to underestimating the connection of H II regions. Choosing a lower threshold value might overestimate the connectivity. Comparing values of V_3 at higher and lower threshold values can be used as an indication of the sufficiency of the resolution of the simulation. In the remainder of this work, we will mostly show the evolution of V_3 at the threshold value $x_{\rm th} = 0.5$ of the oversampled data fields and indicate cases where V_3 is highly dependent on the threshold value. Since the extrema of V_3 of different simulations can vary quite a bit, we choose to plot the function $f(V_3) = \mathrm{Re}\sqrt{V_3} - \mathrm{Im}\sqrt{V_3}$ instead of just V_3. In the interval $[V_3^{\rm max}, V_3^{\rm min}] \rightarrow [\mathrm{f}(\mathrm{V}_3^{\rm max}), f(V_3^{\rm min})]$, f is bijective (i.e. the function has an inverse function); therefore, we continue to refer to it as V_3.

4 BOX SIZE AND RESOLUTION

In this section, we investigate the effect of the simulation volume size on the simulation and the effect of the resolution on our analysis methods. We compare our fiducial simulation to a simulation with the same source properties but in a bigger volume, 163Mpc_g8.7_130S. Before we do so, we analyse a smoothed version of the data of our fiducial simulation to test the effect of the resolution on our analysis methods. We replace the ionization fraction data in each cell with the average over a three cell width volume centred on the cell in question, that is, an average over 27 cells. We will refer to this as three-cell smoothing. This results in a resolution similar to the one in the 163-Mpc simulation. It should be kept in mind that smoothing over three cells does not remove all structure smaller than three cells.

In Section 3, we introduced three measures of size distribution and one estimate for the average bubble size. In Fig. 10, we plot

[7] V_3 of the original density field shows an asymmetry between isolated regions and isolated cavities (for details see Appendix C). A Gaussian smoothing with $\sigma \sim 3$ cells would be necessary to account for this. This removes all small-scale structure; therefore, V_3 is substantially reduced. It also removes extreme over- and underdensities which is why the V_3 curve gets narrower. Using subgrid sampling enhances cells with intermediate densities and therefore changes the distribution away from Gaussian distribution. Therefore, we see deviations from the expected curve for a Gaussian random field, which has $|V_3^{\rm min}|/|V_3^{\rm max}| = 1/[2\exp(-3/2)] \sim 2.2$, as can be calculated, for example, with equation (14) in Schmalzing & Buchert (1997).

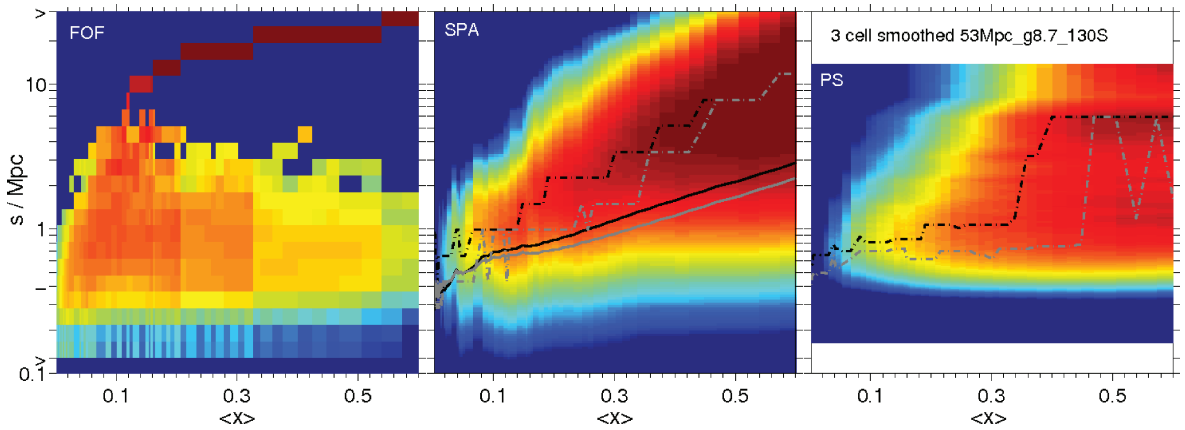

Figure 10. Colour plots of the evolution of size distributions for the three-cell smoothed data of simulation 53Mpc_g8.7_130S. The left-hand panel shows the FoF distribution (colour coded as in Fig. 4). The middle panel shows the SPA (colour coded as in Fig. 5) and its peaks (black dot–dashed line) together with the $3V/A$ estimate (black solid line). The right-hand panel shows the PS (colour coded as in Fig. 6) and its peaks (black dot–dashed line). For comparison, the grey lines show the corresponding measures of the fiducial simulation. Indicated on the ordinates are the cell and simulation volume size for the 53-Mpc simulation (>) and the cell size of the 163-Mpc simulation volume (−).

all four measures as a function of the global ionization fraction for the smoothed version of 53Mpc_g8.7_130S. We also show curves of the peaks of the SPA and the PS. As a reference, these same curves (including the $3V/A$ estimator) for the fiducial simulation are included as grey lines. We first concentrate on the $3V/A$ estimate. As can be seen in the middle panel of Fig. 10 (comparing the two solid lines), above a global ionization fraction $\langle x \rangle \sim 0.1$, the smoothed version yields larger values for $3V/A$. However, the difference is never greater than 20 per cent.

The effect on the SPA distribution (same panel) is mainly a reduction in contribution from scales below 0.5 Mpc. Additionally, the peak of the SPA (compare dot–dashed lines in the same panel) is slightly shifted towards larger scales for the smoothed data.

A somewhat contrary effect can be seen in the FoF size distribution: the contribution from scales below $s \sim 0.3$ Mpc is enhanced in the smoothed data. This can be explained as follows. If a larger ionized structure is elongated (i.e. no structure in two-dimensions) and very inhomogeneous in its ionization fraction, then three-dimensional smoothing would break up the structure in smaller parts.

In the right-hand panel of Fig. 10, we show the PS of the three-cell smoothed data, its maximum curve and the maxima from the fiducial simulation without smoothing. It can be seen, similar to the SPA distribution, that power on scales below $s \sim 0.5$ is removed. Also, it can be seen that at higher global ionization fraction, the distinct peak at scales around 0.8 Mpc diminishes, while the peak at $s \sim 6$ Mpc is as pronounced as in the unsmoothed data.

Since smoothing reduces the small scales and therefore reduces the critical (vertex/edge) H II/H I region connections, oversampling the smoothed data does not change V_3 more than 10 per cent. In Fig. 11 it can be seen that the form of the evolution of V_3 for the fiducial simulation stays roughly the same even for an 11-cell smoothing of the data. However, since the smaller scales are smoothed out, the total amplitude of V_3 is reduced.

Equipped with an idea about which effects can be due to the changed resolution, we now turn to the larger volume simulation. In Fig. 12, we plot all four size measures for simulation 163Mpc_g8.7_130S. We concentrate first on the $3V/A$ size estimate [see the middle panel of that figure (black solid line) and compare it to the $3V/A$ estimate of the fiducial simulation (grey

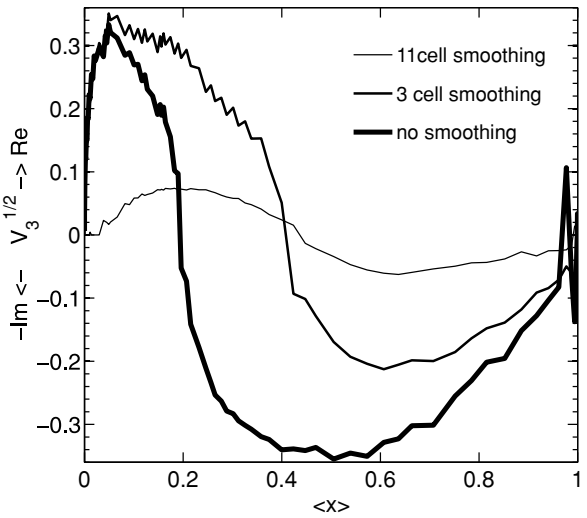

Figure 11. Evolution of V_3 for smoothed versions (degree of smoothing as indicated in the figure by line thickness) of the fiducial simulation at the threshold value $x_{\rm th} = 0.5$. Note the similarity of the behaviour of the curves for different smoothing lengths.

solid line)]: except for very low global ionization fractions ($\langle x \rangle \leq 0.08$) where the estimate for the fiducial simulation is of the order of the cell size of the 163-Mpc simulation volume, the two curves almost coincide up to a global ionization fraction $\langle x \rangle \sim 0.3$, after which the scale in the 163-Mpc simulation grows faster.

The SPA distribution shows a similar behaviour to $3V/A$: below ionization fractions $\langle x \rangle \sim 0.08$, the SPA peaks of the fiducial simulation are at scales comparable to the cell size of the 163-Mpc simulation, while the peaks of 163-Mpc simulation are slightly larger (compare the dot–dashed lines in the same panel). The fiducial simulation also shows a wider distribution with contributions from smaller as well as from larger scales (see the left-hand panel in Fig. 5). Between $\langle x \rangle \sim 0.08$–0.3 the evolution of SPA distribution of the two simulations is very similar. At larger global ionization fractions, the scale of the SPA peak is growing faster in the 163-Mpc simulation.

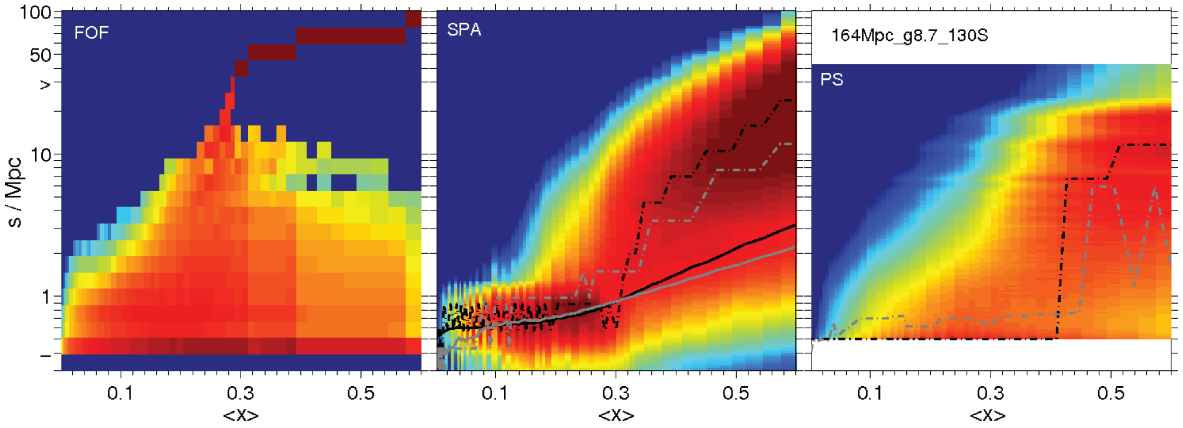

Figure 12. Colour plots of the evolution of size distributions for simulation 163Mpc_g8.7_130S, from the left-hand to right-hand side: FoF, SPA (including $3V/A$, solid black line) and PS. Colour coding and line styles have the same meaning as in Fig. 10.

The PS also shows that, below global ionization fractions $\langle z \rangle \sim 0.3$, despite the different resolution, the simulations with different simulation volumes agree well. At global ionization fractions $\langle x \rangle \geq 0.4$, there is considerable power on scales that are not captured in the 53-Mpc simulation which might explain the shift found by the other size distribution estimates. The PS suggests that the 163-Mpc simulation captures the most relevant scales involved in reionization (i.e. H II region sizes up to roughly $\langle x \rangle \sim 0.5$; H I region sizes above this) since there is little power on scales above $s \sim 30$ Mpc. A notable difference between the simulations is the lack of the peak at scales around 0.8 Mpc in the large simulation volume. As found earlier by the smoothing test, this may be a resolution effect. The peak at scales $s \sim 6$ Mpc is not as clear in the 163-Mpc volume as in the 53-Mpc volume. After $\langle x \rangle \sim 0.5$, it shifts to larger scales.

The FoF size distribution (left-hand panel of Fig. 12 and left-hand panel of Fig. 4) of the two simulations looks at first sight very different. It can be easily understood why: the smallest scale of H II regions in the small simulation volume is smaller than that in the large simulation volume. Looking at the cell-volume limits which are indicated on the abscissa, it can be seen that the additional population of small-scale H II regions present in the 53-Mpc simulation is below the cell-size of the 163-Mpc simulation and therefore below its resolution limit. All those H II regions are partly ionized in the large simulation volume. Therefore, some of them which are more ionized than $x_{\rm th} = 0.5$ appear as an additional population in the FoF distribution of the large simulation volume at scales of its cell size. At 10 per cent global ionization fraction, it can be seen that the 53-Mpc simulation has slightly larger scales than the 163-Mpc simulation, $s \sim 4$ Mpc and $s \sim 5$ Mpc, respectively. Partly ionized cells that are ionized below the threshold value in the larger simulation volume and therefore do not count as belonging to the H II region cannot account completely for this difference in size. This slight mismatch in size between large and small simulation volume might be an artefact from our implementation of suppression: since we suppress all sources inside a cell that has a mass-averaged ionization fraction $\bar{x}_{\rm m}$ larger than 10 per cent, the volume in which sources are suppressed can be overestimated in simulations with larger cell sizes.

While the size distribution in the small simulation volume shows a gap after $\langle x \rangle \sim 0.1$, the gap emerges first at $\langle x \rangle \sim 0.25$ in the large simulation volume. This is because a single region in any of the bins that are empty in the small simulation volume but populated in the large one would already exceed the contribution it makes in the small volume. This sampling effect was already mentioned in the previous section.

At 30 per cent global ionization fraction, the ionized volume of the single large connected region in the 163-Mpc simulation is approximately 10 per cent of the total simulation volume which is larger than the size of the 53-Mpc volume. Similarly, the volume of the largest connected ionized region in the 53-Mpc simulation is also about 10 per cent of the total volume. The fact that the largest connected region is a constant fraction of the simulation volume already at 30 per cent ionized fraction suggests that this region pervades the whole simulation volume. This statement is strengthened by the Euler characteristic of these simulations: V_3 is already highly negative at $\langle x \rangle \sim 0.3$ (for the 163-Mpc simulation, this is only true for lower threshold values, see the left-hand panel of Fig. 13). It should be noted that V_3 of the 163-Mpc simulation shows very similar evolution to V_3 of the 53-Mpc simulation (for a low threshold value for the 163-Mpc volume). The fact that V_3 in the large simulation volume is highly dependent on the threshold value shows that the resolution is not sufficient to use V_3 as a reliable analysis tool: the ambiguity as to whether regions are connected or not is too high, as can be seen comparing the curves for different threshold values in the left-hand panel of Fig. 13. However, it can be seen that the effect of including 'lost' photons is much smaller in the

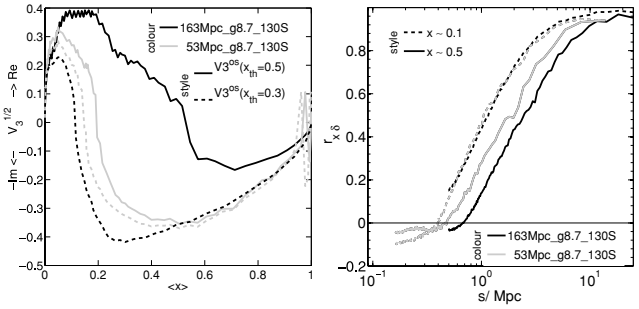

Figure 13. Left-hand panel: evolution of the Euler characteristic V_3 at the threshold values $x_{\rm th} = 0.5$ and 0.3 as indicated in the figure (by line style) for both g8.7_130S simulations, grey lines indicating the 53-Mpc simulation and black lines the 163-Mpc simulation. Right-hand panel: cross-correlation of the density field with ionization fraction of both g8.7_130S simulations (with the same colour coding as in the left-hand panel) at two different global ionization fractions as indicated in the figure (by line style).

large simulation volume: relatively fewer photons travel distances longer than a box distance in the large simulation volume.

The cross-correlation between ionized fraction and density at low global ionization fractions is almost identical for both simulation volumes as the thin lines in the right-hand panel of Fig. 13 show. It differs more at higher global ionization fractions where it shifts towards larger scales for the 163-Mpc simulation, probably indicating that the scales dominating the ionization field at that global ionization fraction exceed the size of the 53-Mpc simulation.

5 PHYSICAL PARAMETERS

Our efficiency parameter g_γ is a product of the efficiency of star formation, production of ionizing photons per stellar atom (related to the initial stellar mass function) and the escape fraction of the photons from the galactic halo into the IGM. All these quantities are not very well constrained at present. Also the efficiency of suppression due to Jeans mass filtering can be different from the simple on–off function as implemented in our simulations with suppression (cf. McQuinn et al. 2007; Mesinger & Dijkstra 2008; Okamoto, Gao & Theuns 2008). To study the effect of our simplified suppression model, we consider in this section some extreme scenarios and use the methods described above to investigate the effect on the scales and the topology of the emerging H II regions.

5.1 Minimum mass of haloes hosting sources with escaping ionizing radiation

In this subsection, we investigate how a change in the source population affects the simulation. In simulations 53Mpc_uvS_1e9 and 53Mpc_g10.4_0, only haloes more massive than 10^9-$M_\odot$ host sources that emit ionizing radiation into the IGM. The former simulation is constructed such that the number of released ionizing photons in every time-step (after the formation of the first massive haloes) is the same as for our fiducial simulation. The sum of all photons that were released in the fiducial simulation by low-mass haloes up to the time at which the first massive halo is forming is emitted additionally in the first time-step after which the first massive source has formed. Since the number of forming haloes increases exponentially, the fraction of additionally released photons in this first time-step is only about half of the total released photons at that time-step. As pointed out in Section 2, the resulting source efficiency is variable with time, shown in Fig. 1. This also means that the minimum number of photons released by one source during one time-step is decreasing with increasing $\langle x \rangle$. Therefore, also the minimum size for H II regions decreases to $\langle x \rangle \sim 0.25$. This can be seen most clearly in the FoF size distribution (Fig. 14, left-hand panel) and in the PS (Fig. 14, right-hand panel). To avoid this effect we performed simulation 53Mpc_g10.4_0 which has a different ionization history from our fiducial simulation, but the source efficiency of the high-mass sources is chosen such that overlap occurs at roughly the same time, as can be seen in Table 1.

The FoF size distribution shows that individual H II regions grow larger before merging with the largest H II region in both the 53Mpc_uvS_1e9 simulation and the 53Mpc_f10.4_0 simulation than in the fiducial one; the gap in the distribution is smaller. This is due to the greater average distance between high-mass sources. The space in between the large H II regions is neutral, without any ionized spots. Therefore, each individual H II region can grow bigger before merging.

Below global ionization fractions $\langle x \rangle \sim 0.2$, the evolution of sizes in the 53Mpc_uvS_1e9 simulation is dominated by the first H II regions emerging around the highly efficient first sources. At higher global ionization fractions, the size evolution is very similar to simulation 53Mpc_g10.4_0. Therefore, we concentrate in the following on the 53Mpc_g10.4_0 simulation.

Compared to our fiducial simulation, the $3V/A$ estimate of simulation 53Mpc_g10.4_0 (middle panel of Fig. 15) suggests an average bubble scale about a factor of 3 greater at all global ionization fractions we consider here. Also the SPA distribution clearly shows this shift to larger scales. This is best visible when comparing the peak scales (dot–dashed curves in the same panel). The PS (Fig. 15, right-hand panel) reveals that it is only a shift to bigger scales below global ionization fractions of about 20 per cent. The H II regions that form first seem to be larger than the ones in the fiducial simulation. Later, it is rather a lack of small scales; notably the peak at scales $s \sim 0.8$ Mpc is absent. This is not surprising as we identified the peak to be due to the suppression of sources in low-mass haloes. The suppression is responsible for halting the growth of the H II regions formed by these sources completely. The peak at scales $s \sim 6$ Mpc is still there. However, there is more power on scales that are not captured by the 53-Mpc simulation volume.

The Euler characteristic for simulation 53Mpc_g10.4_0, see light grey lines in the left-hand panel of Fig. 18 (shown later), is in total much flatter than the Euler characteristic for the fiducial simulation. Since we saw in the FoF distribution and the PS that there is not

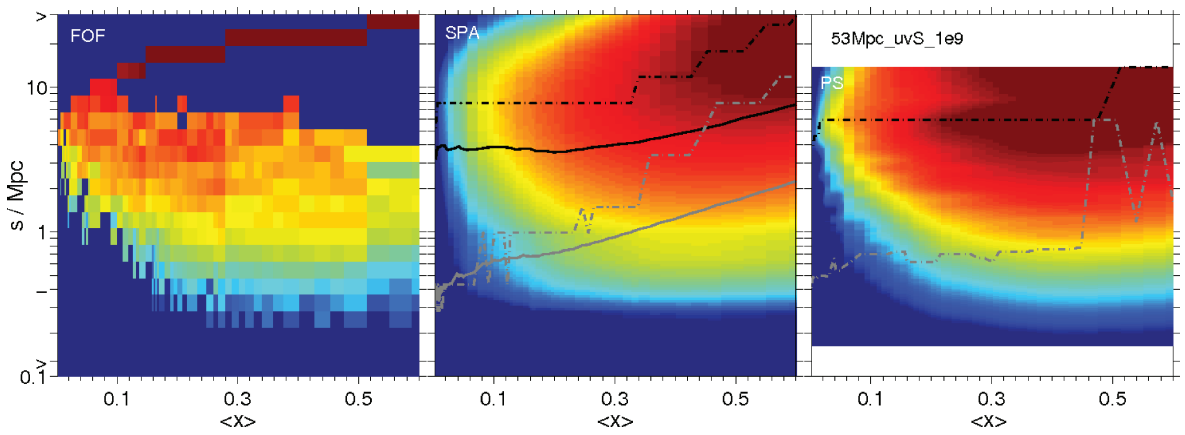

Figure 14. Colour plots of the evolution of size distributions for simulation 53Mpc_uvS_1e9, from the left-hand to right-hand panel: FoF, SPA (including $3V/A$, solid black line) and PS. Colour coding and line styles have the same meaning as in Fig. 10.

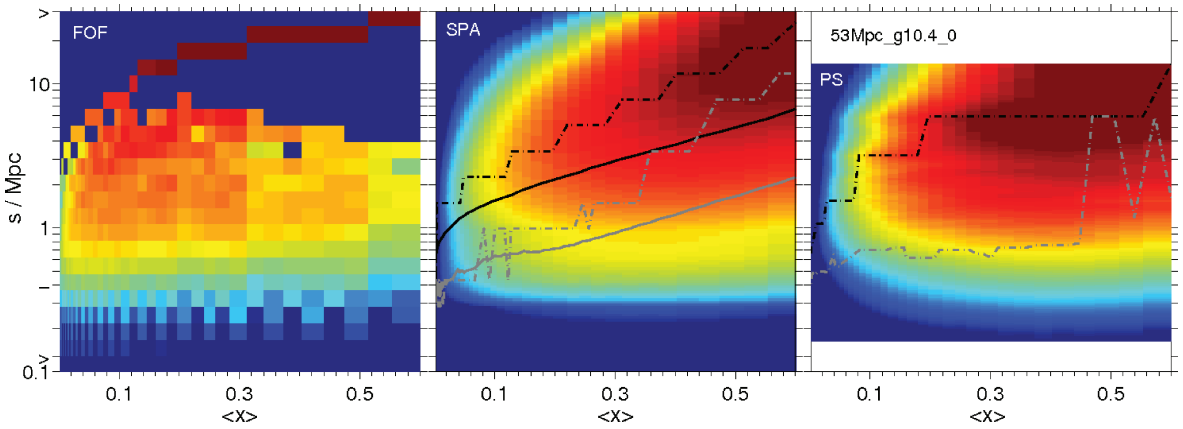

Figure 15. Colour plots of the evolution of size distributions for simulation 53Mpc_g10.4_0, from the left-hand to right-hand panel: FoF, SPA (including $3V/A$, solid black line) and PS. Colour coding and line styles have the same meaning as in Fig. 10.

much contribution from scales that are hardly resolved, this is very unlikely to be due to unresolved scales. We therefore conclude that the bigger H II regions around rare sources result in a less-complex topology with fewer tunnels and cavities. We saw above that feeding back diffuse photons into the volume affects V_3 at high global ionization fractions. The fraction of those photons for simulation 53Mpc_g10.4_0 is already 0.2 at 80 per cent global ionization fraction. Therefore, the evolution of V_3 beyond $\langle x \rangle \sim 0.8$ might be dominated by the effect of these photons, as described in Section 3. It can be seen that V_3 for the low threshold value is at some points considerably different from the value at $x_{\rm th} = 0.5$. However, since we plot the square root of V_3, the differences at values close to 0 are amplified. The actual difference is never greater than 20 per cent of the maximum value.

5.2 Source suppression versus low efficiency

To test the effect of source suppression in regions where the IGM is ionized, we compare our fiducial simulation (with instantaneous complete suppression of sources in low-mass haloes in ionized regions) to two simulations without suppression: 53Mpc_g8.7_130, which has the same source efficiencies, but which ends much earlier due to the many more released photons, and 53Mpc_g0.4_5.3, which has substantially lower source efficiencies to end at roughly the same time as the fiducial simulation.

The comparison of the FoF size distributions between models 53Mpc_g8.7_130 and 53Mpc_g0.4_5.3 (see the left-hand panels in Figs 16 and 17) shows that the model with the lower source efficiencies shows more very small H II regions than the fiducial simulation, similar to 53Mpc_g1.7_8.7S. The simulation with the same source efficiencies as the fiducial simulation but without suppression shows less-small H II regions than the fiducial simulation, because each individual source forming is active longer and so continuously grows its H II region. Also, clustered sources in the same or neighbouring cells support the growth of their joint H II region.

The SPA distribution, see middle panels of Figs 16 and 17 for the higher and lower efficiency simulations without suppression, respectively, shows a very similar evolution. The rate at which the average size grows seems to be the same, but the scale is shifted towards larger scales for simulation 53Mpc_g8.7_130 by about a factor of 1.5. Also, the $3V/A$ size estimates suggest an almost constant shift to larger scales.

The power spectra, see the right-hand panels of the same figures, show more power on small scales (below $s \sim 0.5$) and less power on large scales (above $s \sim 6$) for simulation 53Mpc_g0.4_5.3 than for simulation 53Mpc_g8.7_130. However, up to global ionization fraction $\langle x \rangle \sim 0.5$, the peak at scales around $s \sim 6$ Mpc is present in both simulations. The peak at scales $s \sim 0.8$ Mpc is absent in both simulations.

It should be noted that the size distributions found by all three methods as well as the $3V/A$ size estimator of the 53Mpc_g8.7_130

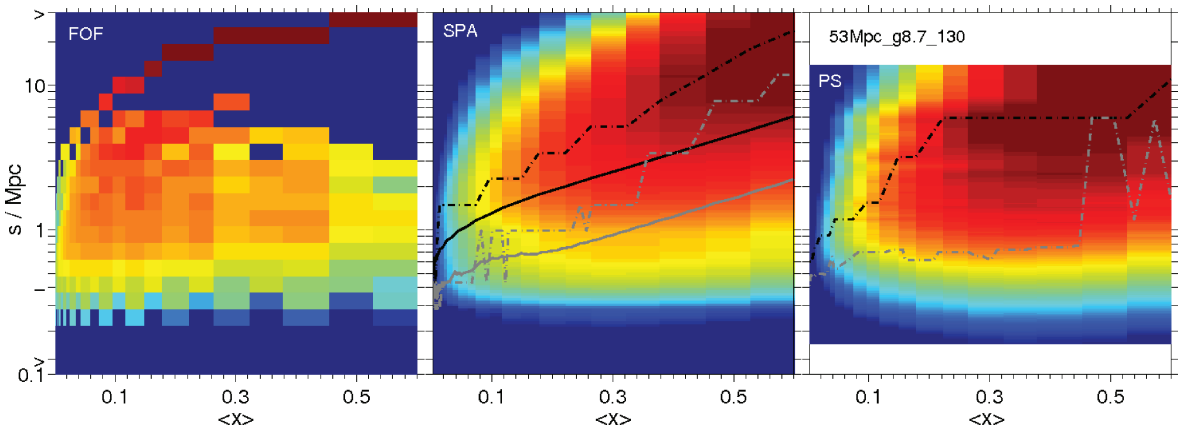

Figure 16. Colour plots of the evolution of size distributions for simulation 53Mpc_g8.7_130, from the left-hand to right-hand panel: FoF, SPA (including $3V/A$, solid black line) and PS. Colour coding and line styles have the same meaning as in Fig. 10.

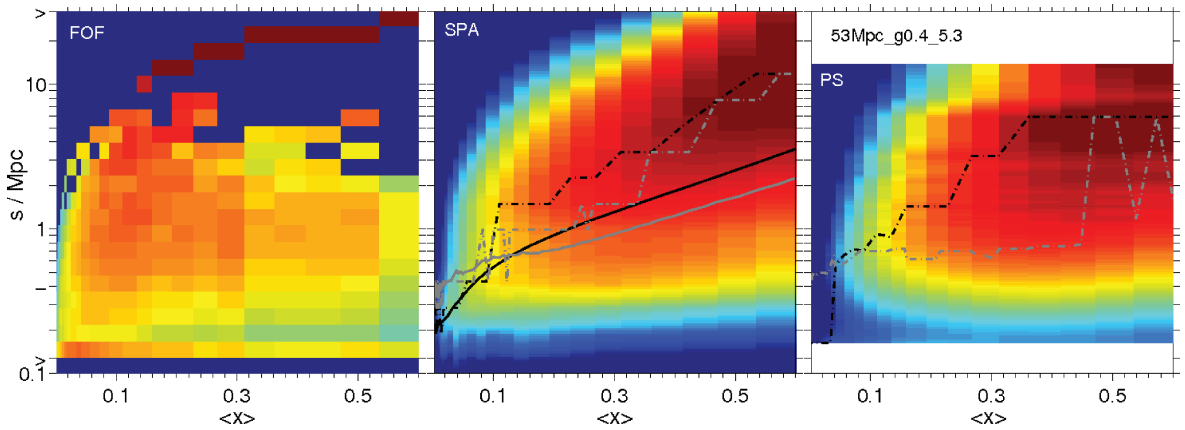

Figure 17. Colour plots of the evolution of size distributions for simulation 53Mpc_g0.4_5.3, from the left-hand to right-hand panel: FoF, SPA (including $3V/A$, solid black line) and PS. Colour coding and line styles have the same meaning as in Fig. 10.

simulation are very similar to the ones from 53Mpc_g10.4_0. However, there is a very significant shift in time between these two simulations. The reason for their similarity if compared at equal $\langle x \rangle$ might be that most haloes which first reach masses above $10^8\,\mathrm{M}_\odot$ reach masses above $10^9\,\mathrm{M}_\odot$ at accordingly lower redshifts. Therefore, the same haloes hosting sources, which turn on as sources in low-mass haloes in the former simulation, turn on as sources in more massive haloes at a later time. This means that if the suppression of sources is not important, the sources 'shaping' reionization are the ones in haloes with the lowest mass that can form luminous sources.

The Euler characteristic (left-hand panel in Fig. 18) shows that V_3 never becomes negative for both simulation 53Mpc_g0.4_5.3 (dark grey lines) and simulation 53Mpc_g8.7_130 (black lines): there are many more disconnected H II regions than neutral tunnels through the ionized regions. For a lower threshold value, $x_{\rm th} = 0.3$, V_3 goes mildly negative. The high dependence of simulation 53Mpc_g8.7_130 on the threshold value is somewhat surprising since the smallest H II regions are larger than for the fiducial simulation. However, the total number of H II and H I regions is small (only a few hundred compared to a few thousand for the fiducial simulation); therefore, a few critical connections are enough to introduce a strong dependence of V_3 on the threshold value. For the 53Mpc_g0.4_5.3 simulation, it can further be seen that the maximum V_3 is about a factor of 4 larger (at a low threshold value, which means most probably overestimating the connections of regions) than for the fiducial simulation. There are more disconnected H II regions due to their smaller minimum sizes. Simulation 53Mpc_g8.7_130 reaches the same global ionization fraction as simulation 53Mpc_g0.4_5.3 at a much higher redshift, at a time when fewer haloes have formed. The maximum V_3 is smaller for the 53Mpc_g8.7_130 simulation, because the individual H II regions grow bigger and merge earlier in terms of the global ionization fraction. However, the big differences between V_3 at different threshold values show that these simulations do not have sufficient resolution; therefore, the ambiguity of connections is too high.

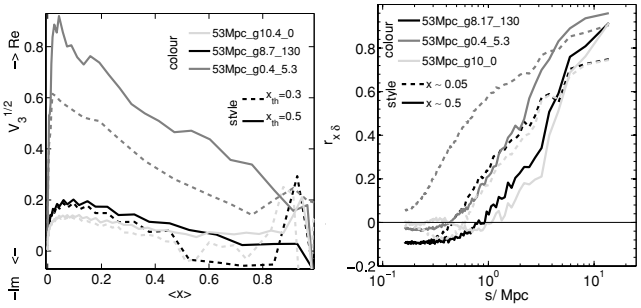

Figure 18. Left-hand panel: V_3 of simulations 53Mpc_g10.4_0, 53Mpc_g8.7_130 and 53Mpc_g0.4_5.3, as indicated in the figure (by line colour) at the threshold values $x_{\rm th} = 0.5$ and 0.3, as indicated in the figure (by line style). Right-hand panel: cross-correlation coefficient for the same simulations at different $\langle x \rangle$, as indicated in the figure (by line style).

Fig. 18 (right-hand panel) shows that the correlation between ionized fraction and overdensity at small global ionization fractions, here represented by $\langle x \rangle \sim 0.05$, is flatter for simulations without suppression, or simulations without any suppressible sources, like simulation 53Mpc_g10.4_0: on large scales, the correlation is lower than for simulations with suppression like our fiducial simulation and on small scales, relatively larger. This behaviour can be interpreted together with the results from the Euler characteristic in the following way: the lack of suppression leads to earlier break outs of the ionizing radiation into the low-density regions between low-mass sources which reduces the number of neutral tunnels and lowers the cross-correlation on larger scales. At the same time, not suppressing sources in partly ionized regions leads to complete ionization of that region which increases the cross-correlation on smaller scales.

At higher global ionization fractions, here represented by $\langle x \rangle \sim 0.5$, these differences disappear because almost all sources in low-mass haloes are suppressed in the simulations with suppression and the reionization process is dominated by the sources in high-mass haloes.

McQuinn et al. (2007) tested the effect of suppression for the case of equally-efficient high- and low-mass sources. However, their simulations do not resolve haloes below $10^9\,\mathrm{M}_\odot$. They use an analytic prescription to include unresolved haloes above the H I atomic cooling mass. Among other things, they found that even their most drastic (instantaneous) suppression model (complete suppression of sources in low-mass haloes) yields an ionization field with similar morphology to a simulation without suppression (their simulations F3 and S1, respectively). Additionally they tested a simulation with higher efficiencies for low-mass sources but without suppression (their model S2). To realize this they chose a mass-dependent source efficiency factor. Very roughly, this translates into

$(10^8/10^9)^{-2/3} \approx 5$ times more efficient low-mass ($10^9 > M/\mathrm{M}_\odot \geq 10^8$) than high-mass ($M/\mathrm{M}_\odot \geq 10^9$) sources in terms of our step-function efficiency assignment method (our fiducial model has 15 times more efficient sources in low-mass haloes). They found that the effect of boosting the efficiency of low-mass sources on ionization field morphology is rather small. From these two tests (F-set versus S1 and S1 versus S2), they concluded that suppression, even in the case of highly-efficient low-mass sources, does not affect the morphology of the ionization field. We can confirm that the ionization field morphology does not change much if the efficiency of low-mass sources is boosted, as long as the total photon output of the least-luminous sources that form the smallest H II regions is held roughly constant (compare, for example, 53Mpc_g10.4_0 and 53Mpc_g8.7_130, Figs 15 and 16, respectively). However, comparing our fiducial simulation (with suppression) to simulations 53Mpc_g8.7_130 and 53Mpc_g0.4_5.3 (both without suppression), we find large differences in the topology and in the average size distributions of ionized regions, as discussed above. This is most probably due to the early break-out of H II regions formed around sources in low-mass haloes in the case of no suppression and high low-mass halo source efficiency.

6 CONCLUSIONS

We have explored different methods for characterizing the scales and topology of complex ionization fraction fields produced by simulations of cosmic reionization. For characterizing the length-scales or sizes of H II regions, we used three methods that give a distribution of scales: the FoF method, the SPA method and the PS of the ionization fraction field. In addition, we proposed a single-valued measure of the average size of H II regions given by the ratio of the volume to the surface of all regions. For characterizing the topology, we employed the Euler characteristic or third Minkowski functional, V_3, of the ionization fraction field.

The nature of the size distribution of H II regions can be viewed to be a matter of definition. Applying a literal definition leads to the FoF approach, in which the H II regions are considered to be connected regions of space. Because the topology of reionization can be quite complex, as seen from the Euler characteristic, this definition does not lend itself easily to analytical modelling, and connecting the FoF size distribution to other scale estimators, such as the PS, is by no means trivial. For the FoF method, what is lost in its complexity is gained in the detailed description of the reionization process that it provides. Although most of the volume is already at quite low global ionization fractions contained in one large connected region, there is a wealth of information contained in the number and sizes of the smaller bubbles, which only occupy a small fraction of the volume. As we found in Section 4, the FoF size distribution is affected by resolution in terms of cell size and one has to take this into account when interpreting the results and comparing simulations with different resolutions. In principle, the FoF method yields the maximum size for isolated ionized regions, before they start to merge into the largest one. However, in practice, this scale is dependent on the sampling of the distribution function and therefore on the size of the simulation volume.

The SPA method, on the other hand, gives distributions which are much smoother and can more easily be connected to analytical models (Zahn et al. 2007). The results are more sensitive to the large-scale H II regions which constitute the main contribution to the global ionization fraction. Due to its averaging nature, it washes out the details. Consider, for example, a collection of two types of spheres with scales $s_1 = a$ and $s_2 = b > a$; the SPA method will only reveal the two distinct scales if $a/b \leq 1/3$. Also, the SPA alone tends to substantially underestimate the sizes of H II regions, as shown in Fig. A1 by our toy model. For using it as a size estimator at par with other methods, the SPA scales should be multiplied by a factor of 4.

When the universe is mostly neutral, the peak of the ionization PS is related to the size distribution of *ionized* regions. For a single top-hat sphere, the first peak in the PS is related to its radius by $k_{\mathrm{max}} = 2.46/r$ and we choose to use $2.46/k$ as a size estimator when comparing to the results of other methods. The PS produces size distributions roughly comparable to those from the SPA method. However, the advantage of the PS over the SPA method is that it does not wash out the details of the distribution. As mentioned earlier, of all size estimators discussed in this paper, the PS is the one most related to upcoming observations as one component in the expansion of the 21-cm PS (e.g. Furlanetto et al. 2006).

The ratio of the zeroth and first Minkowski functionals can be used to define the mean radius of H II regions, the $3V/A$ estimate. This estimate is a surface weighted average. It generally gives results consistent with the maximum of the SPA, and when it falls below that, there is a large fraction of small bubbles (which dominate the surface).

The Euler characteristic V_3 of the ionization fraction field offers a rich description of the evolution of the topology of reionization. Taking our fiducial simulation as an example, in the early stages of reionization, the value of V_3 is positive as the topology is dominated by a large number of isolated H II regions. However, already beyond global ionization fractions of roughly 20 per cent, V_3 becomes highly negative, indicating a complex topology of connected H II regions with tunnels. This is consistent with the distribution from the FoF method, which shows that already at $\langle x \rangle \sim 0.3$ the main contribution to ionized fraction comes from only one large connected region which pervades most of the simulation volume.

As the ionization fronts around stellar sources are quite thin, ideally, V_3 should not depend much on the chosen threshold value and the most interesting aspect is the change in V_3 with time. In this sense, topology studies of H II regions differ from those of density fields, where the variation in V_3 with the threshold value is used to characterize the field at a given time. However, in practice, the resolution of the ionization field may not be sufficient to achieve sharp fronts, and partially ionized cells will occur. The result is different values of V_3 for different threshold values and even different evolutions of V_3 at different threshold values. More seriously is the interaction of this effect with the definition of connectivity/adjacency used when calculating the Euler characteristic. We proposed a new test for establishing how robust the derived values of V_3 are to a change in adjacency. In this, one compares the answer with the value obtained for a field and threshold value which have their sign inverted. Using this we showed that subsampling or smoothing is generally required to obtain consistent results and that for fields with a large fraction of partially ionized cells, it can be difficult to get consistent results.

We subsequently applied the size estimators and Euler characteristic to study differences and similarities between different reionization simulations. Comparing identical simulations in two different volume sizes, 163 and 53 Mpc, shows that below global ionization fractions of 30 per cent the average scales of H II regions are roughly the same for both simulations. Beyond that the size distributions in the larger volume start to contain scales beyond those available in the smaller one. Another manifestation of this is that the largest connected region found by the FoF method for both simulation volume sizes is 10 per cent of each of the simulation volumes already at 30 per cent global ionization fraction. Therefore, this largest H II

region is about a factor of 30 larger in the large simulation volume: a region of this size does not fit into the 53-Mpc simulation volume.

Even earlier there are differences between the two FoF distributions showing the absence of H II regions with volumes of a few hundred Mpc^3 in the small box. This is because relatively isolated overdensity regions (surrounded by larger voids) are missing in the small box due to numerical variance. Since the contribution from those scales is very small, the effect on the average scales is negligible. In general, simple size estimates may be biased due to missing scales (e.g. intermediate scales missing in the small box due to the smaller sampling volume and small scales missing in big box due to resolution). If one is not interested in very small scales, then the lower resolution in the big box appears not to be a problem. The fact that the position of the peak of the PS at all times (global ionization fractions) is well below the box size scale for the 163-Mpc box indicates that no larger simulation boxes are needed to follow the evolution of the peak position.

Comparing simulations with and without suppression (either with only high-mass sources or with sources in low-mass haloes not suppressed in ionized regions) shows that the ones without suppression typically have a much less complex ionization fraction field topology and a more steady growth of average H II region sizes. We thus find significant differences between the cases with and without suppression. For the simulations with sources only in high-mass haloes, this can be explained as follows: the individual H II regions can grow much bigger before merging, due to the larger average distances between high-mass sources. For the simulation without suppression and high-efficiency sources, a similar argument holds, but the whole process takes place at much earlier redshifts. For the simulation without suppression and with low-efficiency sources, the explanation is again similar, but now applied to smaller scales instead of at earlier times. This similarity between the cases without suppression is due to the statistical nature of the density field. If suppression is not important, the sources in haloes with the lowest mass still capable of forming sources are the ones shaping reionization.

By imposing an external photon budget on an independently evolved source population, one can, in principle, separate the effect of the source population from that of the reionization history. However, by necessity, this implies the evolution of the source efficiencies, which, in the case we studied, seriously affected the evolution sizes of H II regions. Up to a global ionization fraction $\langle x \rangle \sim 0.2$, the size distribution is dominated by the size of H II regions generated by the first generation of sources. In the later stages of reionization, the morphology of the ionization field is very similar to a simulation with a fixed source efficiency for high-mass sources.

As outlined in the Introduction, we concentrated on the analysis of the ionization fraction fields and its evolution. Applying the various analysis methods to the future observations of the redshifted 21-cm signal is, in principle, possible, but requires sufficient sensitivity to image the signal at different frequencies. The first generation of telescopes is not expected to be able to do this, but the planned SKA[8] should be. Compared to the simulation results, the observations will have the additional complications of noise and limited spatial resolution (below even that of our 163-Mpc simulation). As we have shown, resolution effects should be treated with care, especially for the Euler characteristic, and noise peaks can obviously also bias the topology determination. Still, characterizing the morphology of H II regions in the data will be important as they trace the mass and thus the emerging cosmic web. We leave the application of the various size/scale and topology estimates to mock observational data to a future paper.

[8] http://www.skatelescope.org

ACKNOWLEDGMENTS

We are grateful to Thomas Buchert for providing us with the code used to compute Minkowski functionals. A significant fraction of the radiative transfer simulations were run on Swedish National Infrastructure for Computing (SNIC) resources at HPC2N (Umeå, Sweden). The authors acknowledge the Texas Advanced Computing Center (TACC) at The University of Texas at Austin for providing HPC resources that have contributed to the research results reported in this paper (URL: http://www.tacc.utexas.edu). This work was supported in part by Swedish Research Council grant 2009-4088, NSF grant AST 0708176, NASA grant NNX07AH09G, Chandra grant SAO TM8-9009X, and NSF TeraGrid grants TG-AST0900005 and TG-080028N.

REFERENCES

Alvarez M. A., Abel T., 2010, preprint (arXiv:1003.6132)
Alvarez M. A., Busha M., Abel T., Wechsler R. H., 2009, ApJ, 703, L167
Choudhury T. R., Haehnelt M. G., Regan J., 2009, MNRAS, 394, 960
Ciardi B., Scannapieco E., Stoehr F., Ferrara A., Iliev I. T., Shapiro P. R., 2006, MNRAS, 366, 689
Crociani D., Mesinger A., Moscardini L., Furlanetto S., 2011, MNRAS, 411, 289
Davis M., Efstathiou G., Frenk C. S., White S. D. M., 1985, ApJ, 292, 371
Fan X. et al., 2006, AJ, 132, 117
Furlanetto S. R., Zaldarriaga M., Hernquist L., 2004, ApJ, 613, 1
Furlanetto S. R., McQuinn M., Hernquist L., 2006, MNRAS, 365, 115
Furlanetto S. R., Oh S. P., Briggs F. H., 2006, Phys. Rep., 433, 181
Gleser L., Nusser A., Ciardi B., Desjacques V., 2006, MNRAS, 370, 1329
Gnedin N. Y., Fan X., 2006, ApJ, 648, 1
Gott III J. R., Dickinson M., Melott A. L., 1986, ApJ, 306, 341
Gunn J. E., Peterson B. A., 1965, ApJ, 142, 1633
Harker G. et al., 2010, MNRAS, 405, 2492
Iliev I. T., Scannapieco E., Shapiro P. R., 2005, ApJ, 624, 491
Iliev I. T., Mellema G., Pen U.-L., Merz H., Shapiro P. R., Alvarez M. A., 2006a, MNRAS, 369, 1625
Iliev I. T., Mellema G., Pen U.-L., Merz H., Shapiro P. R., Alvarez M. A., 2006b, MNRAS, 369, 1625
Iliev I. T., Mellema G., Shapiro P. R., Pen U.-L., 2007, MNRAS, 376, 534
Iliev I. T., Shapiro P. R., Mellema G., Merz H., Pen U., 2008a, TeraGrid '08, preprint (arXiv:0806.2887)
Iliev I. T., Mellema G., Pen U.-L., Bond J. R., Shapiro P. R., 2008b, MNRAS, 384, 863
Komatsu E. et al., 2009, ApJS, 180, 330
Komatsu E. et al., 2011, ApJS, 192, 18
Lee K., Cen R., Gott J. R. I., Trac H., 2008, ApJ, 675, 8
McQuinn M., Lidz A., Zahn O., Dutta S., Hernquist L., Zaldarriaga M., 2007, MNRAS, 377, 1043
Mecke K. R., Buchert T., Wagner H., 1994, A&A, 288, 697
Mellema G., Iliev I. T., Pen U.-L., Shapiro P. R., 2006a, MNRAS, 372, 679
Mellema G., Iliev I. T., Alvarez M. A., Shapiro P. R., 2006b, New Astron., 11, 374
Merz H., Pen U.-L., Trac H., 2005, New Astron., 10, 393
Mesinger A., Dijkstra M., 2008, MNRAS, 390, 1071
Mesinger A., Furlanetto S., 2007, ApJ, 669, 663
Mesinger A., Furlanetto S., Cen R., 2011, MNRAS, 411, 955
Miralda Escudé J., Haehnelt M., Rees M. J., 2000, ApJ, 530, 1
Ohser J., Nagel W., Schladitz K., 2002, in Mecke K., Stoyan D., eds, Morphology of Condensed Matter. Springer-Verlag, Berlin, p. 275
Okamoto T., Gao L., Theuns T., 2008, MNRAS, 390, 920
Oke J. B., 1966, ApJ, 145, 668
Penzias A. A., Wilson R. W., 1965, ApJ, 142, 419

Press W. H., Flannery B. P., Teukolsky S. A., Vetterling W. T., 1992, Numerical Recipes: The Art of Scientific Computing, 2nd edn. Cambridge Univ. Press, Cambridge
Prochaska J. X., O'Meara J. M., Worseck G., 2010, ApJ, 718, 392
Santos M. G., Amblard A., Pritchard J., Trac H., Cen R., Cooray A., 2008, ApJ, 689, 1
Schmalzing J., Buchert T., 1997, ApJ, 482, L1
Schmalzing J., Kerscher M., Buchert T., 1996, in Bonometto S., Primack J. R., Provenzale A., eds, Proc. Int. School Phys. Course CXXXII, Dark Matter in the Universe. IOS Press, Oxford, p. 281
Shapiro P. R., Giroux M. L., 1987, ApJ, 321, L107
Shapiro P. R., Giroux M. L., Babul A., 1994, ApJ, 427, 25
Shin M., Trac H., Cen R., 2008, ApJ, 681, 756
Trac H., Gnedin N. Y., 2009, preprint (arXiv:0906.4348)
Willott C. J. et al., 2007, AJ, 134, 2435
Zahn O., Lidz A., McQuinn M., Dutta S., Hernquist L., Zaldarriaga M., Furlanetto S. R., 2007, ApJ, 654, 12
Zahn O., Mesinger A., McQuinn M., Trac H., Cen R., Hernquist L. E., 2010, preprint (arXiv:1003.3455)
Zaldarriaga M., Furlanetto S. R., Hernquist L., 2004, ApJ, 608, 622

APPENDIX A: SPHERICAL AVERAGE SIZE DISTRIBUTION OF A LOGNORMAL DISTRIBUTION

The SPA method was described by Zahn et al. (2007). In this technique, each cell in the computational volume is considered to be in an ionized region if a sphere centred on that cell has a mean ionized fraction greater than a given threshold, usually $x_{\rm th} = 0.9$. The size of the H II region to which it belongs is taken to be the largest such sphere for which the condition is met.

In the following, we assume that gas is either fully ionized or fully neutral, and that all ionized bubbles are non-overlapping spheres with a volume-weighted distribution $\mathrm{d}P/\mathrm{d}R$, so that $P(R + \mathrm{d}R) - P(R)$ is the fraction of the ionized volume that lies within bubbles with radii between R and $R + \mathrm{d}R$. What bubble distribution, $\mathrm{d}P_{\rm sm}/\mathrm{d}R$, would be obtained by using the SPA method? To simplify further, we will take the threshold for the SPA, $x_{\rm th}$, to be arbitrarily close to unity, so that a point is considered to be within an ionized sphere of a given radius only if *all* the matter in that sphere is ionized. For a single ionized sphere of radius r, $\mathrm{d}P_{\rm sm}(R)/\mathrm{d}R$ is the surface of a sphere with radius $r - R$, normalized by the integral of the surface of spheres with radii from 0 to r: $\mathrm{d}P_{\rm sm}(R)/\mathrm{d}R = 3(r - R)^2/r^3$. If we define this as $W(r, R)$, then

$$\frac{\mathrm{d}P_{\rm sm}}{\mathrm{d}R} = \int_R^\infty \mathrm{d}r\, W(r, R) \frac{\mathrm{d}P}{\mathrm{d}r}, \tag{A1}$$

is the bubble size distribution obtained by the SPA method for the real distribution $\mathrm{d}P/\mathrm{d}R$. The lower limit of the integral is R because only spheres which are larger than R can contribute to the SPA bubble distribution at R (because $x_{\rm th} \to 1$); the largest ionized sphere that can be drawn around any given point is always smaller or equal in radius to the actual ionized sphere in which it lies.

Shown in Fig. A1 are $r\,\mathrm{d}P/\mathrm{d}r$ and the corresponding $R\,\mathrm{d}P_{\rm sm}/\mathrm{d}R$ for three lognormal distributions of bubble sizes:

$$\frac{\mathrm{d}P}{\mathrm{d}\ln r} = \frac{1}{\sqrt{2\pi\sigma^2}} \exp\left\{-\left[\frac{\ln(r) - \ln(\langle r\rangle)^2}{2\sigma^2}\right]\right\}, \tag{A2}$$

with different σ. As can be seen from the figure, the SPA tends to change the true bubble distribution in two ways. First, it smooths the actual bubble distribution with the kernel $W(r, R)$. Secondly, it lowers the value of the mean bubble radius, $R_{\rm av} = \int R\mathrm{d}P/\mathrm{d}R$. In our simple toy model, the mean bubble size obtained by the SPA method is always 1/4 of the actual one. Our toy model is admittedly crude,

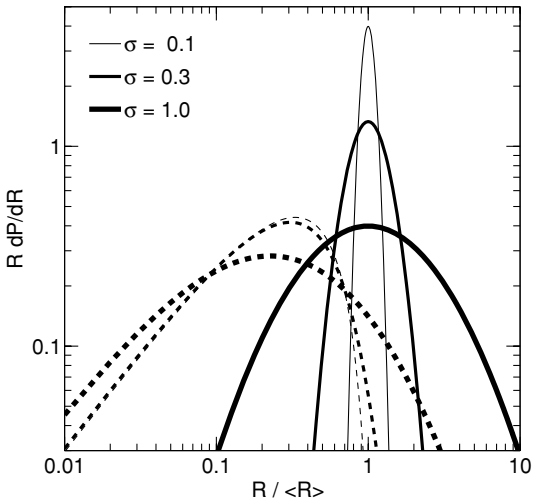

Figure A1. SPA method applied to three lognormal distributions of non-overlapping spherical H II regions. The right-hand (solid) curves are the actual lognormal distributions given by equation (A2) for different values of σ, while the left-hand (dashed) curves show the result which would be obtained on the same distribution using the SPA method. As $\sigma \to 0$ and $\mathrm{d}P/\mathrm{d}R$ approaches a δ function, $\mathrm{d}P_{\rm sm}/\mathrm{d}R$ approaches the kernel function $W(R, \langle R\rangle)$.

most notably in the assumption of a threshold $x_{\rm th} = 1$ and spherical H II regions. A lower value of $x_{\rm th}$ would allow small pockets of neutral gas to be attributed to large ionized regions. In fact, for the case where $x = 1$ and 0 in ionized and neutral regions, respectively, lower values of $x_{\rm th}$ lead to an overestimate of the volume which is ionized, leading to a violation of the normalization condition,

$$\int_0^\infty \mathrm{d}R \frac{\mathrm{d}P}{\mathrm{d}R} = x_{\rm v}. \tag{A3}$$

In most cases, this overestimate is not very large. A lower value of $x_{\rm th}$ would also yield larger H II regions, but this effect has been shown to be rather modest (Zahn et al. 2007). The assumption of spherical symmetry is a conservative one, however, in the sense that it provides a lower limit to how much the SPA method underestimates the 'true' H II region sizes. This is because the SPA method is sensitive to the smallest dimension of the region in which it lies: the radius is larger than the smallest dimension, the part of the sphere lying in that direction would lie outside the region and the average ionized fraction would no longer be above the threshold for the region to be considered ionized.

APPENDIX B: ADDITIONAL SIZE MEASURE

Mesinger & Furlanetto (2007) used another technique to characterize sizes of ionized (and neutral) regions in their binary ionization fields: they chose a large number of random points; for each point, they checked if it was ionized (neutral); from each ionized (neutral) point, they chose a random direction and measured the distance from this point to the nearest ionized–neutral (neutral–ionized) transition boundary along that line of sight. In the following, we use a method similar to the one in Mesinger & Furlanetto (2007). However, instead of choosing a random direction, we, for simplicity, only choose between the three principal axes in one of the two possible orientations. The differences in size distribution obtained with this method only matters for very large and rare H II regions. Small regions should be abundant enough that the orientation should not

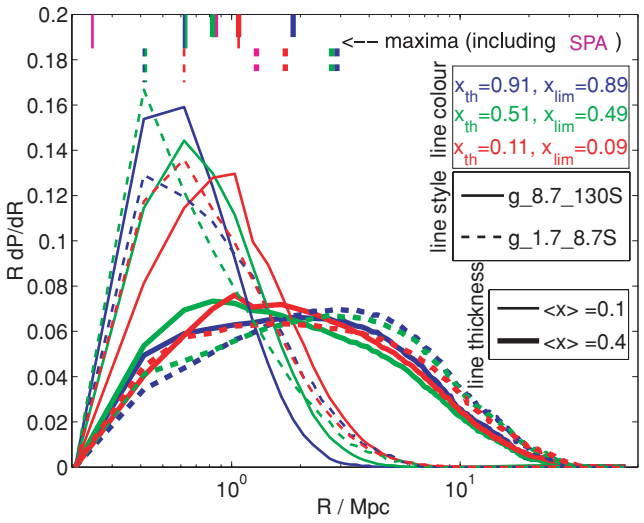

Figure B1. Size distribution curves for simulations g8.7_130S (solid lines) and g1.7_8.7S (dashed lines) using a method similar to the one described in Mesinger & Furlanetto (2007) with three different combinations of the parameters $x_{\rm th}$ and $x_{\rm lim}$ (line colour) at two different global ionization fractions (line thickness). Also indicated are the maxima of the curves and the maxima of the SPA for the same simulations at the same global ionization fractions. Note the large effect of the choice of the parameters $x_{\rm th}$ and $x_{\rm lim}$ on the position of the curve maximum. Note also the shift of the maxima of the SPA towards smaller scales. The maximum of SPA for simulation g1.7_8.7S at a global ionization fraction $\langle x\rangle \sim 0.1$ is at 0.1 Mpc and therefore not visible in this plot.

play a dominant role. Since we have to deal with continuous ionization fields, we have to introduce two parameters: above which ionization fraction is a random point ionized? and what is the limit for the transition boundary along the line of sight? In the following, we consider a point as ionized if its ionization fraction is above $x_{\rm th}$; we count each point along the line of sight ionized as long as its ionization fraction is above $x_{\rm lim}$. In Fig. B1, we plot the size distribution curves obtained with this method for the two simulations we use in Section 3, 53Mpc_g8.7_130S (our fiducial simulation, solid lines) and 53Mpc_g1.7_8.7S (dashed lines) at two different global ionization fractions, $\langle x\rangle \sim 0.1$ (thin lines) and $\langle x\rangle \sim 0.4$ (thick lines). Qualitatively, we find the same result as with the other size measures: initially, the size distribution peaks earlier for 53Mpc_g1.7_8.7S; at higher $\langle x\rangle$, the typical size seems to be larger in this simulation than for the fiducial simulation.

With respect to the peak position of the (uncorrected) SPA, especially at low global ionization fraction, the peak of this size distribution is shifted towards larger scales. This is consistent with the findings in Appendix A and the fact that the size distribution of a single sphere, found with this method, would peak at the radius of the sphere; therefore, this method yields in theory better results than the SPA. However, the disadvantage is the dependence on two parameters if the field of investigation is not a binary field. We tested the effect of these parameters (compare different colours in Fig. B1) and found large variations for different parameter combinations.

APPENDIX C: ON THE CALCULATION OF THE EULER CHARACTERISTIC

The estimation of V_3 of a three-dimensional field sampled on a finite set of grid points is dependent on the chosen adjacency pair, if the structure is of the same order as the cell sizes of the grid. An adjacency pair is for example (26, 6) which means that cells above the threshold (foreground cells) have 26 neighbours and cells below the threshold (background cells) have six neighbours. Because of this dependence on the choice of adjacency pair, we choose to oversample the data to avoid differences in the treatment of isolated/connected H II and isolated/connected H I regions. This introduces a stronger dependency on the choice of the threshold value.

For calculating the Euler characteristic V_3, we use part of a program developed by T. Buchert and J. Schmalzing (Schmalzing & Buchert 1997). The algorithm we use counts the vertices (V), edges (E), faces (F) and lattice cells (C) of the foreground cells and calculates V_3 according to equation (10) in Schmalzing & Buchert (1997):

$$V_3 = V - E + F - C. \tag{C1}$$

In terms of adjacency, this is equivalent to assigning 26 neighbour cells to any foreground cell and six neighbour cells to any background cell. This adjacency pair ensures the three-dimensional Jordan curve theorem (which basically means that an edge connection of foreground cells cannot at the same time be a connection for background cells). Ohser, Nagel & Schladitz (2002) showed that this adjacency pair is complementary which means that V_3 of the background is the same as that of the foreground. If the structure in the data cube has contributions smaller or of the same size as that sampled by the grid cells, then structure of lower dimensions than three can arise. This can cause inconsistencies in the approximation of V_3 of the set sampled at the grid points, resulting in a violation of the complementarity. This is, for example, visible in the (V_3, $\delta_{\rm th}$) plot in Fig. 9: the first peak is mainly due to disconnected underdense regions which are below the density threshold value $\delta_{\rm th}$. If two of those regions are connected via an edge or a vertex, then they count as two disconnected 'cavities' since those cells are background cells and have only six neighbours. The second peak is somewhat smaller than the first one (although theoretically the peaks should be equal). This peak is mostly due to disconnected overdense regions that are above the threshold value $\delta_{\rm th}$ and therefore have 26 neighbours each. Overdensities that are connected via an edge or a vertex count as one connected region; therefore, their contribution to V_3 is smaller.

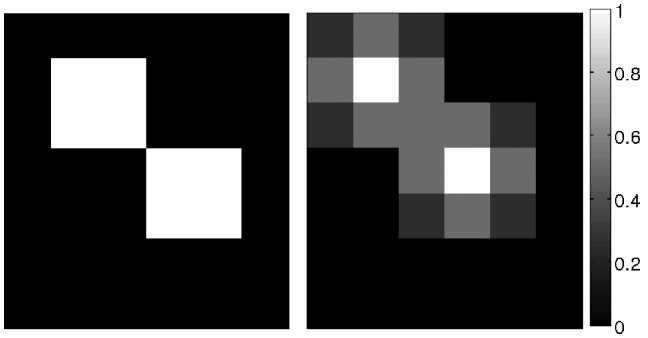

Figure C1. Two-dimensional example to demonstrate the effect of oversampling the data: original structure (left-hand panel) compared to the result from oversampling (right-hand panel). While the original structure counts as one connected region independent of the threshold value ($x_{\rm th} \in (0, 1)$), the structure in the right-hand panel counts as two disconnected regions if $x_{\rm th} > 0.5$ and as one connected region otherwise. If the entries would be inversed (multiplied by -1), the structure in the left-hand panel would count as two disconnected cavities, while the structure in the right-hand panel would have the same dependence on the threshold value as before: the cavities count as disconnected if $|x_{\rm th}| > 0.5$ and as one connected cavity otherwise.

Ohser et al. (2002) showed that the bias of the approximation depends on the choice of adjacency. Inverting the data cube of ionization fraction, so that at every grid point, $x' = -x$, computing V_3' at $x'_{\rm th} = -x_{\rm th}$ and then comparing $V_3'(x'_{\rm th})$ to $V_3(x_{\rm th})$ is equivalent to changing the adjacencies from (26/6) to (6/26).

For example, consider a 3^3 cube $C1$, with $C1(1, 1, 2) = C1(2, 2, 2) = 1$ and 0 everywhere else and a cube $C2 = -C1$. Then, $V_3(C1, x_{\rm th}) \neq V_3(C2, -x_{\rm th})$: $V_3(C1, x_{\rm th} = l) = 14 - 23 + 12 - 2 = 1$, where $l \in (0, 1)$ (round brackets denoting open intervals), while $V_3(C2, x_{\rm th} = -l) = (\vartheta) - (\xi) + (\zeta) - (\varphi - 2) = 2$, where ϑ, ξ, ζ and φ are the numbers of vertices, edges, faces and lattice cells of the cube $C(1{:}\,3, 1{:}\,3, 1{:}\,3) = 0$, respectively, the sum of which is 0 since periodicity is assumed.

Therefore, we use $V_3(-x, -x_{\rm th})$ as a check for how good the approximation of V_3 is. To minimize the asymmetry due to the chosen adjacency, we oversample the data. For the example of the cubes $C1$ and $C2$ from above, this means that $V_3(C1, x_{\rm th} = l) = V_3(C2, x_{\rm th} = -l) = 1$ for $l \in (0, 0.5)$ and $V_3(C1, x_{\rm th} = l) = V_3(C2, x_{\rm th} = -l) = 2$ for $l \in [0.5, 1)$. Obviously, this results in a higher dependency on the chosen threshold value, as this simple example demonstrates (see also Fig. C1 for a two-dimensional example).

As a second example, we present here the Euler characteristic of the fiducial simulation and simulation 53Mpc_g1.7_8.7S to demonstrate the effect of oversampling and the choice of the threshold value. As explained above, calculating $V_3(-x_{\rm th})$ of the inverted field (the data field multiplied by -1, in the following indicated by a '$-$') is equivalent to changing foreground to background cells and vice versa. This is the same as changing the adjacencies. Therefore, comparing $V_3(+, x_{\rm th})$ to $V_3(-, -x_{\rm th})$ is a test for the dependence on adjacencies.

Fig. C2 demonstrates the dependence on the chosen adjacency pair when analysing the data fields without smoothing or oversampling [compare $V_3(+, x_{\rm th} = 0.5)$ to $V_3(-, x_{\rm th} = -0.5)$ for both simulations] and the lower dependence on the chosen adjacencies after oversampling the data [compare $V_3^{\rm os}(+, x_{\rm th} = 0.5)$ to $V_3^{\rm os}(-, x_{\rm th} = -0.5)$]. It also demonstrates the relatively low dependence on the threshold value $x_{\rm th}$ for the fiducial simulation and the high dependence on $x_{\rm th}$ for simulation 53Mpc_g1.7_8.7S [compare $V_3^{\rm os}(+, x_{\rm th} = 0.5)$ to $V_3^{\rm os}(+, x_{\rm th} = 0.3)$].

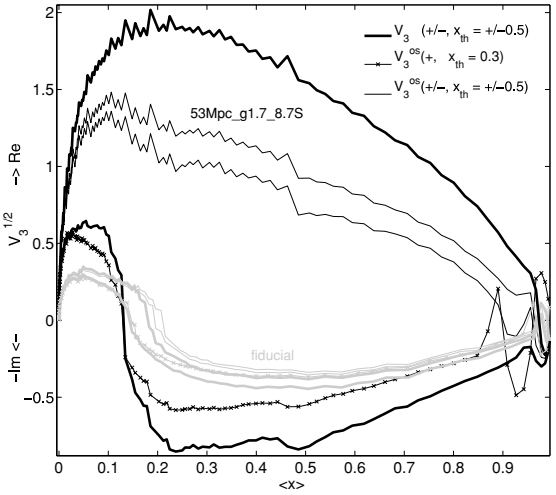

Figure C2. Evolution of the Euler characteristic V_3 for the original field of the fiducial simulation (lower grey thick line) and simulation 53Mpc_g1.7_8.7S (lower black thick line) at the threshold value $x_{\rm th} = 0.5$. The upper thick lines are the corresponding Euler characteristics of the inversed fields at the threshold value $x_{\rm th} = -0.5$. The thin lines correspond to the oversampled fields of the fiducial simulation (lower grey thin line) and simulation 53Mpc_g1.7_8.7S (lower black thin line) at the threshold value $x_{\rm th} = 0.5$. The upper thin lines are the corresponding Euler characteristic of the inversed oversampled fields at the threshold value $x_{\rm th} = -0.5$. The grey (fiducial simulation) and black (53Mpc_g1.7_8.7S) lines with crosses indicate the Euler characteristic of the oversampled fields at the threshold value $x_{\rm th} = 0.3$. Note the good agreement for $V_3^{\rm os}$ ($x_{\rm th} = 0.5$) and $V_3^{\rm os}$ ($x_{\rm th} = -0.5$) and the low dependence on the threshold value for the fiducial simulation.

Others (e.g. Gleser et al. 2006) chose to smooth the data with a Gaussian kernel to remove lower dimensional parts. This has the disadvantage that some of the small-scale structures are suppressed.

This paper has been typeset from a TEX/LATEX file prepared by the author.